Astrocytic RNA editing regulates the host immune response to alpha-synuclein

Karishma D'Sa[*1,2], Minee L. Choi[*1,2,3], Aaron Z. Wagen[*1,2,4,5], Núria Setó-Salvia[1,6], Olga Kopach[7], James R. Evans[1,2], Margarida Rodrigues[8,9], Patricia Lopez-Garcia[1,2,5], Joanne Lachica[1,2,5,10], Jaijeet Singh[1,2], Ali Ghareeb[11], James Bayne[11], Melissa Grant-Peters[4,5], Sonia Garcia-Ruiz[4], Zhongbo Chen[1,2], Samuel Rodriques[11], Dilan Athauda[1,2], Emil Gustavsson[4,5,10], Sarah A. Gagliano Taliun[12,13], Christina Toomey[1,2,5,10], Regina H. Reynolds[4,5], George Young[2,14], Stephanie Strohbuecker[2], Tom Warner[1,6], Dmitri A. Rusakov[7], Rickie Patani[2,15], Clare Bryant[16], David A. Klenerman[8,9], Sonia Gandhi[1,2,5*†], Mina Ryten [4,5,9,17,18*†]

[1]Department of Clinical and Movement Neurosciences, UCL Queen Square Institute of Neurology, Queen Square, London, UK

[2]The Francis Crick Institute, 1 Midland Road, London, UK

[3]Department of Brain & Cognitive Sciences, KAIST, 921 Dehak-ro, Daejeon, Republic of Korea

[4]Department of Genetics and Genomic Medicine, Great Ormond Street Institute of Child Health, University College London, London, UK

[5]Aligning Science Across Parkinson's (ASAP) Collaborative Research Network, Chevy Chase, MD

[6]Reta Lila Weston Institute, UCL Queen Square Institute of Neurology, London, UK

[7]Department of Clinical and Experimental Epilepsy, UCL Queen Square Institute of Neurology, London, WC1N 3BG UK

[8]Department of Chemistry, University of Cambridge, Cambridge, UK.

[9]UK Dementia Research Institute at The University of Cambridge, Cambridge, United Kingdom.

[10]UCL Queen Square Institute of Neurology, University College London, London, UK

[11]Applied Biotechnology Lab, The Francis Crick Institute.

[12]Montréal Heart Institute, Montréal, QC, Canada

28 [13]Department of Medicine & Department of Neurosciences, Université de Montréal,
29 Montréal, QC, Canada.

30 [14]MRC Laboratory of Medical Sciences, London

31 [15]Department of Neuromuscular Disease, UCL Queen Square Institute of Neurology, Queen
32 Square, London, WC1N 3BG UK

33 [16]Department of Veterinary Medicine, University of Cambridge, Cambridge CB3 0ES, UK

34 [17]Department of Clinical Neurosciences, School of Clinical Medicine, The University of
35 Cambridge, Cambridge, UK

36 [18]Department of Genetics, University of Cambridge, Cambridge, UK

37

38 [*] Joint Authors

39 [†] Corresponding Authors

40

Abstract

RNA editing is a post transcriptional mechanism that targets changes in RNA transcripts to modulate innate immune responses. We report the role of astrocyte specific, ADAR1 mediated RNA editing in neuroinflammation in Parkinson's disease. We generated hiPSC-derived astrocytes, neurons and co-cultures and exposed them to small soluble alpha-synuclein aggregates. Oligomeric alpha-synuclein triggered an inflammatory glial state associated with TLR activation, viral responses, and cytokine secretion. This reactive state resulted in loss of neurosupportive functions, and the induction of neuronal toxicity. Notably, interferon response pathways were activated leading to upregulation, and isoform switching of the RNA deaminase enzyme, ADAR1. ADAR1 mediates A-to-I RNA editing, and increases in RNA editing were observed in inflammatory pathways in cells, as well as in post-mortem human PD brain. Aberrant, or dysregulated, ADAR1 responses and RNA editing may lead to sustained inflammatory reactive states in astrocytes triggered by alpha-synuclein aggregation, and this may drive the neuroinflammatory cascade in Parkinson's.

Introduction

Parkinson's disease (PD) is a progressive neurodegenerative condition characterised by the accumulation of intraneuronal aggregates of alpha-synuclein (α-syn) through the brain (*1*). Astrogliosis has been reported in post-mortem Parkinson's brain (*2*–*7*), and in rodent models of synucleinopathy (*8*, *9*), and astrocytes accumulate α-syn inclusions (*10*), raising a role for astrocytes, and astrocyte-mediated immune cascades (*11*), in triggering or driving PD pathogenesis. Astrocytes are an abundant glial cell, essential for neuronal function, and survival through the maintenance of CNS homeostasis via modulation of neurotransmitters and synapse formation, ionic balance, and maintenance of the blood-brain barrier (*12*). Reactive astrogliosis defines a process whereby, in response to pathology, astrocytes undergo changes in transcriptional regulation, biochemical, morphological, metabolic, and physiological remodeling, which ultimately result in a switch from resting to reactive states. The nature of the underlying stimulus (neuroinflammatory vs ischaemic) has defined certain reactive astrocyte states into neurotoxic (so called A1, which promote lipid mediated

71 neuronal death via activated microglia) and neuroprotective (so called A2, which promote
72 neuronal survival and regeneration through neurotrophic factors) (*13*). Reactive
73 transformation can be associated with loss of neurosupportive and homeostatic functions,
74 reduced synapse formation (*14*), alterations in glutamate uptake and recycling (*15*), and
75 dysregulated calcium signalling (*16*). Simultaneously reactive states are associated with the
76 gain of neurotoxic properties (*17*).

77

78 Focusing on PD, there is evidence that A1 astrocytes have been shown to infiltrate brain
79 regions associated with PD, including the striatum(*13*). Astrocytes in these regions express
80 the highest regional levels of immune mediators, such as toll-like receptor 4 (TLR4) and
81 myeloid differentiation primary response 88 (MyD88) , correlating with PD pathology (*18*).
82 Significantly, inhibiting the formation of these A1 astrocytes by blocking microglia-astrocytic
83 cross talk is neuroprotective in mouse models of PD (*19*). Reactive astrocyte substates are
84 likely to be diverse beyond these two states (*14*, *20*), and involve several exogenous and
85 endogenous triggers such as damage-associated molecular patterns (DAMPs) or proteostatic
86 stresses induced by misfolded proteins. Compared to control cell lines, human astrocytic
87 models of PD release increased amounts of pro-inflammatory cytokines in response to α-syn
88 (*21*). Moreover, in response to α-syn fibrils, iPSC-derived astrocytes can assume an antigen
89 presenting function, with upregulation of major histocompatibility complex (MHC) genes and
90 relocation of HLA molecules to the cell surface to present α-syn fibril peptides to neighbouring
91 cells (*21*). This finding, replicated in post-mortem brain samples (*22*), supports the idea that
92 astrocytes may mediate the immune response in the brain.

93 We have recently reported that physiological concentrations of oligomeric α-syn, trigger a
94 TLR4-dependent inflammatory response in murine primary astrocytes (*18*). The small soluble
95 hydrophobic and beta sheet rich aggregates, or oligomers of α-syn are known to be
96 neurotoxic, and trigger cell selective processes that are specific to the structural conformation
97 of the protein (*23*–*26*).

98 Sub-state modelling has been achieved in human iPSC-derived astrocytes and co-cultures
99 (*27*), which enable capture at a molecular level of cell autonomous and non-cell autonomous
100 cascades in pathology. We investigate how human iPSC-derived astrocytes respond to α-syn
101 oligomers (αsyn-O), which downstream response pathways are activated, and how this

102 reactivity affects neurons. We integrate bulk and single-cell transcriptomic, functional and
103 biophysical approaches in five lines of human iPSC-derived (hiPSC-derived) astrocytes (3 in-
104 house and 2 commercial lines), both alone and in co-culture with neurons, to define the
105 molecular response of astrocytes to misfolded α-syn. Finally, identifying innate immune
106 pathways of interest, we explore those pathways in post-mortem brain samples from those
107 with PD.

108 Results

109 Generation and functional characterisation of hiPSC-derived astrocytes and neurons alone 110 or in co-culture

111 We generated hiPSC-derived astrocytes from 5 healthy donors, and cortical neurons from a
112 sixth healthy donor (**Supp table 1**) (*28*). We compared the cellular response to αsyn-O in
113 astrocyte only, neuron only and astro-neuronal cultures (**Figure 1a**). Highly enriched cultures
114 of cortical astrocytes in feeder-free conditions were generated from three in-house lines
115 using an optimised small molecule serum free protocol, and two were purchased
116 commercially, derived through a proprietary serum free protocol (**Figure 1b**). We used the Shi
117 et al., 2012 protocol (**Figure 1b**) to generate highly enriched (>90%) and functional hiPSC-
118 derived cortical neurons from neural precursor cells (*24*, *25*).

119 Immunolabelling with GFAP, an astrocyte-specific marker demonstrated that cultures
120 contained >90% mature astrocytes (**Figure 1c**). hiPSC-derived astrocytes also displayed
121 cytosolic calcium responses on application of ATP as assessed using Fura-2 (**Figure 1d**) (*29*).
122 All lines demonstrated appropriate Na+ dependent uptake of glutamate from the
123 extracellular space, one of the major astrocytic functions that indicates functional activity of
124 Excitatory Amino Acid Transporter 1/2 in hiPSC-derived astrocytes (**Figure 1f(i)**). Together,
125 the ATP-dependent calcium responses and glutamate uptake confirmed generation of
126 functionally mature astrocytes.

127 To investigate how astrocytes affect neuronal function, we generated co-cultures by plating
128 hiPSC-derived cortical astrocytes and neurons in a 1:1 ratio, and cultured for at least 3 days
129 prior to use. The composition of co-cultures was assessed by immunocytochemistry using
130 both MAP2, a neuronal marker, and GFAP, an astrocytic marker (**Figure 1e, 1f(ii)**). The co-

131 cultures contained 55.9 ± 3.4% MAP2 positive cells and 42.9 ± 2.7% GFAP positive cells, while
132 neuronal cultures contained 93.2 ± 1.7% MAP2 positive cells and astrocytic cultures contained
133 90.5 ± 1.3% GFAP positive cells.

134 In order to generate oligomers of α-syn, human recombinant monomeric WT α-Syn was
135 aggregated in the dark at 37°C and 200 r.p.m., for ~7–8 hours. At this time point, the mixture
136 consists of 99% monomeric α-syn, and 1% oligomeric α-syn, with oligomers being small,
137 soluble, and rich in beta sheet structure as characterised previously (*24*, *25*, *30*).

138 Whole cell patch-clamp recording of neurons was performed in neuron only and astro-
139 neuronal cultures to assess the electrophysiological properties and excitability of the cells. In
140 neuron only cultures, neurons (~100 DIV) displayed a relatively depolarised resting membrane
141 potential (*V*rest) compared with age-matched cells in co-cultures (–45.9 ± 2.8 mV, n = 33 vs.
142 –56.0 ± 2.1 mV, n = 34, p = 0.0053, respectively, **Supp figure 1(a,b)**). No significant difference
143 was observed in neuronal capacitance across culture types (C_m: 44.8 ± 3.5 pF, $n = 35$ in
144 cultures and 43.7 ± 3.8 pF, $n = 40$ in co-cultures, $p = 0.843$; (**Supp figure 1c**). Input resistance
145 (**Supp figure 1d**) and the time constant (**Supp figure 1e**) were significantly altered in astro-
146 neuronal cultures. In neuron only cultures, neurons generated a single action potential (AP)
147 in response to current injection, whereas neurons in astro-neuronal cultures generated a train
148 of induced APs in either step-wise depolarising protocol or slow-injecting ramp current (**Supp**
149 **figure 1f**). The parameters of AP spike (threshold, spike amplitude, kinetics) also confirmed
150 that co-cultures altered the neuronal performance. Neurons were more excitable in co-
151 cultures, as a lesser current was required to bring neurons to drive firing (**Supp figure 1g-j**).

152

153

154

155

156

157 **Single-cell RNA-sequencing of astrocyte only, neuron only and astro-neuronal cultures**

158 We used RNA-sequencing to further characterise hiPSC-derived astrocytes and neurons. After
159 120 days of differentiation all cells were harvested with and without αSyn-O stimulation, each
160 with a technical replicate resulting in 44 samples. Using the 'in house' protocol, cultures were
161 sequenced with single-cell technology (astrocyte only, neuron only and astro-neuronal
162 cultures, with and without αsyn-O). Across the integrated single-cell dataset we identified 8
163 cell clusters, which include both astrocytic and neuronal subtypes. Cell types were assigned
164 using a set of previously published and curated marker genes (*31*, *32*). Based on the
165 expression of these marker genes, we identified two astrocytic and six neuronal clusters
166 (**Figure 1g (i,ii)**). Given that hiPSC-derived astrocytic profiles have been previously well
167 characterised by Leng and colleagues (*27*) we initially assessed our clusters for correlations in
168 gene expression globally with the reported iAstrocytes transcriptomic profiles and found they
169 were highly correlated with both of our astrocyte clusters (r = 0.71 and 0.64) (**Figure 1g(iii)**),
170 subsequently referred to as astrocyte cluster 1 (AC1) and 2 (AC2).

171 Given the growing literature on astrocytic subtypes, we investigated the clusters further.
172 Focusing specifically on genes differentially expressed between the clusters (AC1 and AC2),
173 we identified 300 genes of interest (at FDR< 5% and >2-fold change in expression) of which
174 129 were more highly expressed in AC1 and 171 genes which were more highly expressed in
175 AC2 (**Supp table 2**). Interestingly, gene set enrichment analysis of these differentially
176 expressed genes , identified immune and cytokine-related terms amongst genes more highly
177 expressed in AC1. Conversely, genes more highly expressed in AC2 showed enrichment for
178 terms related to morphogenesis, regulation of development and differentiation (**Figure**
179 **1g(iv), Supp table 3**). Furthermore, we noted that the pattern of gene expression in the AC2
180 cluster appeared to resemble that described for neuroprotective astrocytes (**Supp figure 2a**).
181 Thus, we identified 2 subtypes of astrocytes, AC1 and AC2, which differed in terms of their
182 inflammatory and protective transcriptomic profiles.

183

184 **hiPSC-derived astrocytes are reactive to αsyn-O and secrete cytokines**

185 Next, we examined whether hiPSC-derived astrocytes take up αsyn-O using a Fluorescence
186 Resonance Energy Transfer (FRET) biosensor which enables visualisation of oligomers in cells
187 (*25*) We treated hiPSC-derived astrocytes with two populations of fluorescently tagged α-syn
188 (AF488- & AF594-tagged A53T α-syn monomers, total 500 nM) for 5 days, and then measured
189 the intracellular accumulation of α-syn ('total α-synuclein') based on the intensity of AF594
190 through direct excitation with 594 nm irradiation. The formation of oligomer ('FRET') was
191 visualised via the presence of signal from the acceptor fluorophore (AF594) after excitation
192 of the donor fluorophore (488 nm irradiation) (**Figure 2a**). Using this approach, we found total
193 α-syn uptake was higher in hiPSC-derived astrocytes than neurons, while similar levels of de
194 novo aggregates (FRET) were detected in both cell preparations (**Figure 2b**).

195 αsyn-O exposure can cause cell toxicity, and excessive ROS generation in primary astrocytes
196 (*18*). To determine whether hiPSC-derived astrocytes show similar responses, we assessed
197 ROS production using dihydroethidium (DHE) dye which allowed us to robustly measure the
198 rate of oxidation of the dye by cellular superoxide production (*33*). We found that ROS
199 production significantly increased compared to basal levels (normalised to 100%, **Figure 2c**)
200 in hiPSC-derived astrocytes after the application of αsyn-O.

201 Since our previous study showed that αsyn-O treatment triggers an inflammatory response in
202 primary astrocytes with associated increases in cytokine release (*18*), we assessed this
203 phenomenon in hiPSC-derived astrocytes. Following treatment of hiPSC-derived astrocytes
204 with a range of αsyn-O concentrations (100nM – 2uM) overnight, we collected the media and
205 assessed the cytokine profiles using an MSD (V-PLEX Proinflammatory Panel 1)
206 electrochemiluminescence assay kit. We found that αsyn-O treatment of hiPSC-derived
207 astrocytes consistently induced a significant increase in the secretion of a variety of cytokines
208 compared to untreated cultures. Thus, we demonstrated that αsyn-O exposure induces
209 hiPSC-derived astrocytes to become pro-inflammatory (**Figure 2e,f**).

210

211 **Oligomer treatment of hiPSC-derived astrocytes triggers anti-viral inflammatory responses**

212 Next, we used bulk RNA-sequencing to investigate hiPSC-derived astrocyte responses to αsyn-
213 O treatment in more detail. Given that we identified two major astrocytic clusters (AC1 and
214 AC2), we determined whether αsyn-O changes the relative proportions of these cell clusters.
215 With this in mind, we used the tool Scaden (*34*) together with our scRNA-seq data (Materials
216 and methods) to estimate cluster proportions in bulk RNA-Seq data across the whole dataset,
217 noting a high correlation in cell type proportion estimates based on single-cell and Scaden-
218 derived data (**Supp figure 2b**). This approach was based on the colocalization of all astrocytic
219 samples within exploratory principal component analyses based on bulk RNA-seq data, so
220 suggesting that the astrocyte clusters we identified in a subset of samples were in fact present
221 in all. While we found no significant change in astrocyte subtype proportion between basal
222 and αsyn-O treated astrocyte cultures (**Figure 2g, Supp table 4**), significant changes in gene
223 expression and splicing were observed.

224 We identified 2004 genes which were significantly differentially expressed (8.17% at FDR <
225 5% and at least 2-fold change in expression) following treatment of hiPSC-derived astrocytes
226 with αsyn-O, of which 917 were up-regulated and 1087 were down-regulated in the treated
227 astrocytes (**Supp table 5**). Importantly, these up-regulated genes with at least 2-fold change
228 in expression were enriched for those implicated in viral responses, including "defence
229 response to virus", "response to interferon-gamma", "type I interferon signalling pathway"
230 (**Figure 2h, Supp table 6**). These results were highly consistent with the functional data
231 demonstrating a robust cytokine response to αsyn-O treatment . Since splicing analyses have
232 been shown to provide distinct biological information (*35–37*), this form of analysis was used
233 to further characterise hiPSC-derived astrocyte responses to αsyn-O. We identified 707
234 significant differentially spliced intron clusters corresponding to 590 genes (FDR < 0.05,
235 $|\Delta PSI| \geq 0.1$) with significant enrichment for cytoskeletal terms, potentially reflecting the
236 observed morphological changes in astrocytes with oligomer treatment (**Supp figure 3 & supp**
237 **tables 7,8,9**). Morphological changes induced by αsyn-O are evaluated through astrocyte
238 segmentation, followed by quantification of GFAP pixel area and intensity based on the
239 distance from the nuclear membrane. This approach assesses both morphological polarity
240 and intensity gradients (*38*, *39*), providing a detailed understanding of the spatial distribution
241 and intensity changes in astrocytic morphology thus enabling the tracking of reactive
242 astrocytic morphology upon αsyn-O stimulation.

243

244 **hiPSC-derived astrocytes maintain inflammatory states on exposure to αsyn-O in co-culture**

245 First, we studied the functional effects of αsyn-O treatment on astro-neuronal cultures. Media
246 collected from the samples were used to measure a range of cytokines secreted from the cells
247 using an MSD (V-PLEX Proinflammatory Panel 1) electrochemiluminescence assay kit. αsyn-O
248 induced more secretion of a variety of cytokines compared to untreated co-cultures
249 demonstrating inflammatory activation of the co-culture (**Figure 3a**).

250 Previously we have demonstrated that αsyn-O induced an increased level of neuronal death
251 and oxidative stress (*18*, *24*, *25*). Using live-cell imaging, we showed that activated astro-
252 neuronal cultures were associated with higher levels of cell death (**Figure 3b(i)**), and higher
253 levels of ROS production (**Figure 3b(ii, iii)**). Furthermore, patch-clamp recordings performed
254 in co-cultures treated with αsyn-O demonstrated a drop in the *V*rest after treatment (**Supp**
255 **figure 4b**) and increased input resistance (**Supp figure 4c**) in neurons. Neurons also had
256 impaired firing, with a dramatically changed AP waveform. The threshold for AP spike
257 generation was depolarised (**Supp figure 4d,e**), the amplitude was reduced (**Supp figure 4f**),
258 and the spike was significantly extended compared with control astro-neuronal cultures. Thus
259 the proteinopathy appeared to induce an activated inflammatory state of astrocytes, that is
260 associated with loss of the previous neuronal supportive function seen with resting
261 astrocytes. Additionally there are toxic gain-of-function effects in both astrocytes and
262 neurons in co-culture, such as induction of oxidative stress, altered excitability, and neuronal
263 cell death.

264 As before, we also combined single-cell and bulk RNA-sequencing analyses to assess the
265 impact of αsyn-O treatment on cell subtype proportions, gene expression and splicing. We
266 observed a significant increase in the proportion of AC1 (inflammatory) relative to AC2
267 (neuro-protective) astrocytes in αsyn-O treated as compared to co-cultures basally (**Figure 3c,**
268 **Supp table 4**). We noted that there was no significant difference observed in the cell type
269 proportions of AC1 and AC2 in astrocyte only cultures on αsyn-O treatment (**Supp table 4**).
270 Differential gene expression analysis following correction for changes in predicted cell type
271 proportions, identified 774 genes (3.46%, FDR < 5% and at least 2-fold change in expression)
272 with 509 up-regulated and 265 down-regulated in the αsyn-O treated as compared to the co-

273 cultures basally (**Supp table 5**). Similar to the findings on αsyn-O treated astrocytes only, the
274 up-regulated genes with at least 2-fold change in expression were highly enriched for immune
275 response terms (**Figure 3d, Supp table 10**). As observed in the astrocyte only cultures, the
276 terms highlighted were associated with viral infections, such as "defence response to virus"
277 and "type 1 interferon signalling pathway". Furthermore, we noted that gene enrichment
278 ratios for immune-related GO terms were consistently higher in αsyn-O treated co-cultures
279 compared to astrocyte only cultures, suggesting a more prominent inflammatory response to
280 oligomer treatment in co-cultures (**Figure 3e, Supp table 11**).

281 Again, analysis of differential splicing identified distinct biological processes that were related
282 to structural organisation of cells and physical cell interactions, in contrast to gene level
283 expression signals. We identified 502 differentially spliced intron clusters in 414 genes
284 (FDR < 0.05, $|\Delta PSI| \geq 0.1$), with the genes enriched for terms relating to junction assembly and
285 synapse (**Supp table 7**). Finally, we assessed differentially expressed and differentially spliced
286 genes for evidence of enrichment for genes genetically associated with either Mendelian
287 forms of early onset PD and Parkinsonism, or complex PD (*40*, *41*). While we did not see any
288 enrichment of Mendelian genes in astrocyte only cultures, there was significant enrichment
289 amongst all genes that were differentially expressed or differentially spliced (**Supp table 12**)
290 in astro-neuronal cultures. Overall, this suggests that this model is related to PD pathogenesis
291 and uncovers pathways related to PD causation.

292

293 **Oligomer treatment triggers *ADAR* expression and a change in isoform use**

294 αsyn-O treatment of both astrocyte only and astro-neuronal cultures resulted in the
295 activation of pathways most commonly associated with responses to viruses. In both cases,
296 we noted significant increases in the expression of genes such as *MDA5*, *RIG1* and *TLR3* that
297 can sense viral RNA (double-stranded RNA or Z-RNA)(*42–44*) and activate the release of IFN
298 and cytokines (**Figure 4a, Supp figure 5b**). This in turn is known to trigger the up-regulation
299 of a range of genes, including *OAS1*, *PKR* and *ZBP1* to degrade viral RNA, inhibit translation
300 and drive necroptosis respectively, and indeed this up-regulation was identified in αsyn-O
301 treated cultures (**Figure 4a, Supp figure 5b**).

302

303 However, these processes also undergo negative regulation by ADAR, an enzyme which
304 deaminases adenosines on double stranded RNA to inosines (*45*). This conversion reduces the
305 activation of dsRNA sensors by disrupting RNA self-complementarity and so favouring the
306 formation of single-stranded RNA forms, as well as through other direct and indirect
307 modulation of pro-inflammatory pathways (*46–49*). In fact, it is known that biallelic
308 pathogenic variants in ADAR that reduce its editing activity, result in excessive release of
309 interferons and tissue damage, and present as Aicardi Goutieres syndrome (*50*). With this in
310 mind, we noted that αsyn-O treatment of both astrocyte and astro-neuronal cultures resulted
311 in significant increases in *ADAR* expression (**Figure 4a, Supp figure 5c**) of 1.86 and 1.82 fold in
312 the cultures respectively.

313

314 Furthermore, αsyn-O treatment resulted in significant differences in transcript use (**Figure 4b,**
315 **Supp figure 5a**) as detected through splicing analyses. More specifically, we noted a decrease
316 in the use of an exon-exon junction specific to *ADAR*-201 (1:154602627-154627854:-)
317 encoding the ADAR p110 isoform, and a relative increase in the usage of an exon-exon
318 junction (1:154602627-154607991:-) specific to *ADAR*-202 encoding the p150 isoform, which
319 is already known to be under the control of an IFN-sensitive promoter (**Figure 4b, Supp figure**
320 **5a**). Thus, the functional and transcriptomic analyses of astrocyte only and astro-neuronal
321 cultures, suggest that αsyn-O treatment triggers the increased expression of *ADAR* and an
322 increase in the use of the cytoplasmic p150 isoform.

323

324

325 **αsyn-O treatment increases A-to-I editing in astrocyte-containing samples.**

326 We postulated that changes in *ADAR* expression and its isoform use would result in both an
327 increase in A-to-I editing rate and a change in the distribution of A-to-I editing sites. The latter,
328 would be expected as a consequence of the different properties of ADAR's two major
329 isoforms, with the p110 exclusively found in the nucleus and the p150 being largely
330 cytoplasmic (*51*). To investigate this we used the high-depth bulk RNA-seq data we generated
331 across all cultures to identify editing sites, in each case comparing to the reference genome.

332 Focusing on basal conditions, we detected 78,547 editing sites in astrocyte only cultures,
333 103,340 sites in the neuron only cultures, and 100,740 sites in the astro-neuronal cultures
334 (**Figure 5a**). Consistent with the known higher levels of editing in neurons (*52*), we found that
335 the median baseline editing rate at a given site was higher in neuron only (0.208) than in
336 astrocyte-containing cultures (0.054 in astrocyte only, 0.056 in astro-neuronal cultures).
337 Given that astro-neuronal cultures were composed of ~50% neurons, our findings suggest
338 that in the presence of astrocytes editing rates in neurons are lower.

339 This analysis also revealed differences in the distribution of editing sites across cell cultures.
340 In astrocyte only cultures, 50.3-59.5% of editing sites were in exonic regions, with the
341 majority of these located in the 3'UTR (49.6% and 40.9% of editing sites in astrocyte only and
342 astro-neuronal cultures, respectively **Figure 5d**). By contrast, in the neuron only cultures we
343 found that just 25.4% of sites were located in the 3'UTR. Finally, consistent with the known
344 molecular function of *ADAR* we found that irrespective of genic location or culture type, the
345 majority of editing sites (83.6 – 86.6%) were located within repeat regions, of which the vast
346 majority were in Alu regions (93.2 – 94.5%) (**Supp Figure 6c**).

347 As predicted, αsyn-O treatment generated an increase in the number of editing sites in all
348 cultures (15.8% in astrocyte only, 26.2% in neuron only, and 11.1% in astro-neuronal
349 cultures), which was highly significant (chi-squared p-value of $<2x10^{-16}$ for increased exonic
350 proportion in all cases). Similarly, measurement of editing rates at each site demonstrated
351 both a marked increase in the number of new editing sites and editing rate in astrocyte and
352 astro-neuronal cultures, but not neuron only cultures (**Figure 5b**). In contrast, across all
353 cultures relatively few editing sites were lost or had a decrease in editing rate.

354 Furthermore, consistent with a change in transcript usage, αsyn-O treatment was associated
355 with a change in the distribution of editing sites. In astrocyte-containing samples, the sites
356 with increased editing rates were significantly more likely to be in 3'UTRs than sites with
357 decreased editing (p-value $< 2x10^{-16}$ in both astrocyte only and astro-neuronal cultures), while
358 in neuronal monocultures the proportion of sites in 3'UTRs did not change significantly (p-
359 value = 0.17)**.** A similar pattern was observed when exploring the biotype (as defined by
360 Ensembl VEP 93.5) of the transcripts containing a given editing site, with sites identified to
361 have an increase in editing rate in astrocyte-containing cultures being more likely to be

362 located within protein coding transcripts (p-values < $8.2x10^{-8}$ and $2x10^{-16}$ in astrocyte only and
363 astro-neuronal cultures respectively, **Supp figure 6b**). Taken together, these results show that
364 αsyn-O treatment is associated with an increase in the number of editing sites and differential
365 editing rate in astrocyte-containing cultures.

366 Noting that RNA editing can influence gene expression through effects on mRNA stability, we
367 explored the relationship between transcript editing, gene expression and gene function (*53*).
368 We began by identifying all genes that both contained sites with significant differential editing
369 on exposure of cells to αsyn-O treatment, and which had significant differences in gene
370 expression in the same conditions. We found that there was a significant overlap in genes
371 that were differentially edited and differentially expressed in the astrocyte only and astro-
372 neuronal cultures following αsyn-O treatment (Fisher's exact test p-value for astrocytes
373 8.54E-4, co-culture 2.39E-2). Focusing on this gene set, namely genes that were both
374 differentially edited and expressed, we found a significant enrichment for the terms linked to
375 viral infection and immune response in both the astrocyte-containing cultures (**Figure 5e**,
376 **Supp table 13**).
377
378

379 **A-to-I RNA editing is increased in post-mortem PD brains**

380 While A-to-I editing in the human brain is well-recognised and perhaps best characterised in
381 neurons, the molecular machinery for editing is present in all the major cell types. In humans
382 A-to-I editing is catalysed not only by ADAR1 (*ADAR*), but also ADAR2 (*ADARB1*) which
383 primarily edits at conserved sites in the genome (*51*, *53*, *54*). Using publicly available
384 snRNAseq data from human brain, we confirmed the expression of *ADAR* in all major cell types
385 including astrocytes (**Figure 5f)**. In astrocytes, the majority of expression was found in the
386 astrocytic subtype expressing *VIM*, *SOX9* and *FOS*, with 19.4% of these cells expressing *ADAR*.
387 The mean expression of *ADAR* also appeared to be higher in this subgroup, with *ADAR* among
388 the top 500 most expressed genes. This is in keeping with *VIM*-positive astrocytes being
389 immunoreactive, associating with response to toxins, viruses and cytokines, activation of
390 surrounding neurons, projections over extended distances in the CNS, and astro-vascular
391 interactions (*55–57*).

392 To explore whether the changes in A-to-I RNA editing seen in-vitro were also reflected in PD-
393 affected human brain tissue, we explored RNA editing in a publicly available dataset of 5
394 control and 7 PD post-mortem brain samples (*58*). Using high depth RNA-seq data generated
395 from the anterior cingulate cortex, and after controlling for covariates, we found that PD brain
396 samples had significantly higher levels of RNA editing than control samples (beta 0.011, 95%,
397 p $<2.2x10^{-16}$ CI [0.009, 0.012]). This association remained significant in a further analysis,
398 which also included the total number of editing sites per sample (beta 0.007, 95% CI [0.006,
399 0.009]). Next, we assessed the cell type specificity of the editing response. Focusing on genes
400 with the greatest increase in mean editing rate in PD (top 50 genes), we used expression
401 weighted cell type enrichment analysis (*59*) to formally assess the cell type-specificity of this
402 gene set. We found significant enrichments for multiple glial cell types, including OPCs and
403 oligodendrocytes. However, the cell type with the most significant enrichment was the
404 astrocytes (3.8 standard deviations increased from the mean, adjusted p value 0.0014),
405 suggesting that astrocytes are involved in this process in-vivo (**Figure 5g**) though not
406 exclusively.

407

408 ## Discussion

409 Astrocytes are the most abundant glial cells, supporting neuronal health and CNS immune
410 responses through multiple heterogeneous reactive and proliferative states (*60*). Whilst
411 several triggers for these states are well recognised, it remains less clear how different glial
412 states contribute in the context of diseases associated with proteinopathies. Here we
413 generated a platform of human iPSC-derived astrocytes to investigate the intersection
414 between protein aggregation as a trigger for astrocytic state switching in disease. We used a
415 serum-free small molecule approach to generate functionally active astrocytes,
416 demonstrating homeostatic calcium responses, glutamate uptake, and maturation of
417 neuronal function, as well as responses to inflammatory stimulation by canonical microglial
418 triggers (LPS). Adopting single cell sequencing to characterise the molecular identity of the
419 astrocytes revealed two astrocytic subclasses,protective and inflammatory,recapitulating key
420 astrocytic states seen in the CNS and associated with PD (*13*). Furthermore, the transcriptomic
421 signatures of our iPSC-derived astrocytes correlated highly with iPSC-derived astrocytes

422 generated by other groups (*27*). Our cellular platform may therefore be used to model
423 astrocytic states and sub-states, and uncover the mechanisms that underlie them, despite the
424 inherent limitation of their developmental fetal phenotypes (*61*).

425

426 The innate immune response recognizes pathogen- and danger-associated molecular
427 patterns (PAMPS & DAMPS) via pattern recognition receptors (including toll-like receptors
428 (TLRs), and retinoic acid-inducible gene I (RIG-I)-like receptors) (*62–64*). The role of α-syn as
429 a PAMP/DAMP is not well understood. It is currently known that α-syn may be transferred
430 from neurons to astrocytes in vitro (*65*), or from astrocytes to neurons (*66*), and several
431 mechanisms of astrocytic uptake and transfer have been proposed, including endocytosis (*67*)
432 and tunnelling nanotubes (*68*), or via Toll like receptor 2 activation enhancing the uptake of
433 fibrils (*69*). We previously demonstrated that physiological concentrations of oligomers
434 provoke an immunological response that is largely TLR4 dependent, and that glial TLR4-
435 Myd88 signalling in the substantia nigra may be causative in PD pathogenesis (*18*).

436

437 Here, we utilised the same α-syn aggregate species to reveal the downstream consequences
438 of recognition by TLRs, and the underlying mechanisms of astrocytic reactivity driven by
439 protein aggregation. Our data confirms that oligomers are recognised as DAMPS/PAMPs
440 (driven by genes *TLR3, DDX58 (*RIG-I*)).* Typically, this is followed by activation of key
441 inflammatory transcription factors, nuclear factor κB (NF-κB) and interferon regulatory
442 factors (IRFs) that induce the release of type I interferon (IFN). The initial type I IFN release
443 consequently induces the phosphorylation of IRF7, and phosphorylation of STAT2 and STAT1,
444 which forms a complex with IRF9, known as the IFN-stimulated gene factor 3 (ISGF3).
445 Oligomers induce the expression of *NFκB, IRF7, STAT1, STAT2, and ZBP1,* reflecting this
446 pathway in the hiPSC astrocytes. Finally, the DAMPS/PAMPS trigger the activation of the
447 NLRP3 inflammasome that facilitates the activation of caspase-1 and release of
448 proinflammatory cytokines interleukin-1β (IL-1β), IL-18, and pyroptosis, a sequence also
449 triggered by oligomers (*NLRP3, CASP1, IL1B)*. This transcriptomic response was mirrored
450 functionally with the morphological switch to an activated astrocyte, release of inflammatory
451 cytokines, and generation of reactive oxygen species. Moreover, in this reactive state, the
452 astrocytic supportive function of promoting neuronal activity was lost, and neuronal toxicity

453 was induced. Taken together these results suggest a mechanism whereby αsyn-O's can trigger
454 an inflammatory response in astrocytes with resulting glial and neuronal toxicity.

455

456 Intracellular double-stranded (dsRNA), evolutionarily a sign of viral infection, can also act as
457 a DAMP, and dsRNA triggers multiple cytoplasmic receptors including ZBP1, MDA5, OAS, PKR
458 which activate various arms of the innate immune cascade, including NF-κB signalling and the
459 type 1 interferon response. Of the broad changes in gene expression observed in our
460 experimental paradigm, oligomer induced type 1 interferon changes were accompanied by
461 the activation of anti-viral response pathways, with upregulation of the cytosolic double-
462 stranded nucleic acid (dsNA) sensing machinery. This machinery includes activation of the
463 negative regulator ADAR1, an enzyme that performs RNA editing, breaking the homology of
464 dsRNA, and thus dampening the immune response triggered by cytosolic dsNA and type 1
465 interferons (*45*). It is important in responding to cytosolic dsRNA that is endogenous in origin,
466 and not secondary to viral infection. From an evolutionary perspective, this process is
467 especially important in humans, where expansion of retrotransposition of non-coding
468 repetitive elements,especially alu repeats, has markedly increased the amount of
469 endogenous dsRNA within cells (*70*). The importance of the immune-dampening effect of
470 ADAR- p150 is demonstrated in loss of function mutations which result in Aicardi Goutieres
471 Syndrome, an infantile inflammatory encephalopathy which can also cause striatal necrosis,
472 a brain structure implicated in PD (*71*).

473 ADAR1 has two major isoforms, with the p110 exclusively found in the nucleus and the p150
474 being largely cytoplasmic. In the hIPSC astrocytes, we observed promoter switching with the
475 induction of the inflammatory isoform of ADAR1-p150. This resulted in a marked increase in
476 A-to-I RNA editing site number and editing rate per site, most prominently in astrocyte-
477 containing samples. The changes in editing were enriched in 3'UTRs suggesting that treatment
478 with αsyn-O resulted in a higher proportion of editing activity within the cytoplasm, where
479 ADAR1-p150 is known to localise. Furthermore, amongst genes that were both differentially
480 edited and expressed, we found a significant enrichment for terms linked to viral infection
481 and immune response in both the astrocyte-containing cultures. Thus the RNA editing is likely
482 to dampen the inflammatory response to the oligomers in vitro.

483

484 Finally, we explored the role of RNA editing in PD. Using publicly available high depth RNA-
485 seq data generated from the anterior cingulate cortex from control and PD-affected
486 individuals, we found that PD brain samples had significantly higher levels of RNA editing than
487 control samples. Having identified astrocyte specificity of the RNA editing response in vitro,
488 we assessed the cell type-specificity of the editing response in vivo. Genes with the most
489 significant editing in PD were enriched in multiple glial cell types, but most significantly in
490 astrocytes, confirming the role of astrocyte RNA editing in vivo.

491 Our work raises a number of outstanding questions: how do the structural motifs of the
492 oligomers act as danger associated molecular patterns, and trigger the interferon and editing
493 response, and when does this process occur in the natural history of PD? However, most
494 importantly, is A-to-I RNA editing a beneficial compensatory response to the inflammatory
495 cascade, or does it exacerbate neurodegeneration in PD? Finally, whilst there is overlap
496 between RNA editing and the genetic risk of PD (*72*), the role of altered RNA editing in PD
497 remains unknown.

498 The findings here provide new insights into the mechanism by which inflammation may be
499 implicated in PD pathogenesis: specific protein aggregates of α-syn may act as a DAMP to
500 astrocytes, trigger inflammation and interferon like responses, which in turn triggers anti-viral
501 dsRNA responses, leading to activation of RNA editing to dampen proteinopathy induced
502 inflammatory responses. In this work, the disease specific trigger for this mechanism was the
503 beta sheet rich, soluble oligomer of α-syn. However, such mechanisms may also be triggered
504 by viral infections, which are believed to be associated with an increased risk of developing
505 PD (*73*). The identification of dsNA sensing pathways provides a potential convergent
506 mechanism between proteinopathy and viral infections in the pathogenesis of PD.

507

508 # Materials and methods

509 **Aggregation of human recombinant alpha-synuclein**

510 Human recombinant α-Syn Monomeric WT or A53T α-Syn was purified from Escherichia coli
511 as previously described (*74*). Aggregation reactions were carried out using a solution of α-Syn:
512 70 µM in 25 mM Tris buffer supplemented with 100 mM NaCl, pH 7.4 (in the presence of
513 0.01% NaN3 to prevent bacterial growth). The buffer was freshly prepared before each

514 experiment and passed through a 0.02 µm syringe filter (Anotop, Whatman) to remove
515 insoluble contaminants. Prior to incubation, the reaction mixture was ultra-centrifuged at 90k
516 r.p.m. for 1h at 4°C to remove potential seeds. The supernatant was collected and separated
517 in two fractions: one kept at 4°C at all times until use (monomers), and a second incubated in
518 the dark at 37°C and 200 r.p.m., for ~7–8 hours to generate oligomers, and avoid fibril
519 formation. α-Syn was always kept in LoBind microcentrifuge tubes (Eppendorf, Hamburg,
520 Germany) to limit surface adsorption.

521

522 **hiPSc culture**

523 hiPSCs were derived from donors who had given signed informed consent for the derivation
524 of hiPSC lines from skin biopsies as part of the EU IMI-funded program StemBANCC and
525 reprogrammed as described (*75*). Briefly, the Cyto Tune-iPS reprogramming kit (Thermo
526 Fisher Scientific) was used to reprogram fibroblasts through the expression of OCT4, SOX2,
527 KLF4 and c-MYC by four separate Sendai viral vectors. Control 1 (C1) and 2 (C2) were derived
528 by StemBANCC from an unaffected volunteer and control 3 (C3) was purchased from Thermo
529 Fisher Scientific. Control 4 & 5 (C4 & C5) were purchased from Applied Stem Cell. hiPSCs were
530 maintained on Geltrex in Essential 8 medium (Thermo Fisher Scientific) and passaged using
531 0.5mM EDTA.

532

533 **Differentiation of hiPSC into neurons and astrocytes**

534 Differentiation of cortical region-specific astrocytes was performed using a modified protocol
535 based on (*76*, *77*). Briefly, as demonstrated in Fig 1b, hiPSC were differentiated into neural
536 precursor cells (NPCs) using an established protocol (*78*). In order to derive glial precursor
537 cells (GPCs), NPCs were cultured with dual SMAD inhibition for 25-30 days, followed by
538 culturing with the neural induction medium supplemented with 20 ng/ml human FGF-2).(*78*)
539 The passage was performed twice per week (1:2 or 1:3) using Accutase (Cat #A1110501,
540 Thermo Fisher Scientific) by vigorously breaking pellets to remove neuronal cells. Upon the
541 appearance of glial morphology (around day 90 from the neural induction), the GPCs were
542 cultured for 7 days with 10 ng/ml bone morphogenetic protein 4 (BMP4) and 20 ng/ml
543 leukemia inhibitory factor (LIF) which activates the JAK/STAT signalling pathway, refreshing

544 the medium every other day. On the 8th day, BMP4 and LIF were withdrawn, and the GPC
545 were further differentiated for maturation in the neural induction medium without human
546 FGF-2. 3-4 times more passages are required (1:3 or 1:4) until the complete loss of the
547 precursor property, including proliferation.

548

549 For neurons, at around 35 days of induction, cells were dissociated into a single cell using
550 accutase and approximately 150,000number of cells plated either PDL and laminin-coated
551 glass bottom 8-well slide chambers (Ibidi/Thistle, cat No.80826), Geltrex coated 8-well ibidi
552 chambers (cat No. IB-80826) or 96-well plates (Falcon, cat No. 353219). Medium was replaced
553 every 4–5 days and cells were used at 60–90 days after induction.

554

555 **Live-cell imaging**

556 Live-cell imaging was performed using an epi-fluorescence inverted microscope equipped
557 with a CCD camera (Retiga; QImaging) or confocal microscope (ZeissLSM710 or 880 with an
558 integrated metal detection system). For epi-fluorescence inverted microscope, excitation was
559 provided by a xenon arc lamp with the beam passing through a monochromator (Cairn
560 Research) and emission was reflected through a long-pass filter to a cooled CCD camera and
561 digitized to 12-bit resolution (Digital Pixel Ltd, UK) and the data were analyzed using Andor iQ
562 software (Belfast,UK). For confocal microscopes, illumination intensity was limited to 0.1-
563 0.2% of laser output to prevent phototoxicity and the pinhole was set to allow optical slice at
564 approximately 1–2µm. Pre-room temperature warmed HBSS was used as a recording buffer.
565 3–6 fields of view per well and at least 3 wells per group were used to analyze using ZEN,
566 Volocity 6.3 cellular imaging or ImageJ software. All experiments were repeated at least 2-3
567 times with different inductions.

568

569 To measure Reactive Oxygen Species (ROS, mainly superoxide), cells were washed and loaded
570 2uM dihydroethidium (HEt, Thermo Fisher Scientific) in the recording buffer. The recording
571 was performed using an epi-fluorescence inverted microscope equipped with 20x objective
572 after a quick loading in order to limit the intracellular accumulation of oxidized product and
573 the dye was present throughout the imaging. Excitation was set up to 530 nm and emission

574 recorded above 560 nm was assigned to be for the oxidized form, while excitation at 380nm
575 and emission collected from 405nm to 470nm were for the reduced form. The ratio of the
576 fluorescence intensity resulting from its oxidized/reduced forms was quantified and the rate
577 of ROS production was determined by dividing the gradient of the HEt ratio after the
578 application of recombinant α-Syn against basal gradient.

579

580 For [Ca2+]c imaging, Fura-2, AM which is a ratiometric dye with a high affinity for Ca^{2+} was
581 used. The cytosolic Ca2+as well as the rapid transient kinetics and decay times were assessed.
582 5u MFura-2 was loaded for 40 min and then washed twice before imaging. The fluorescence
583 measurement was obtained on an epifluorescence inverted microscope equipped with a 20x
584 objective. [Ca2+] was monitored in a single cell by obtaining the ratio between the excitation
585 at 340nm (high Ca2+) and 380nm (low Ca2+) for which fluorescence light was reflected
586 through a 515nm long pass filter. To trace morphological changes, Fluo4 was used and
587 recorded using confocal microscopy.

588

589 Cell death was detected using SYTOX™ Green(SYTOX, Thermo Fisher Scientific) which is
590 excluded from viable cells but exhibits red fluorescence following a loss of membrane
591 integrity and Hoechst 33342 (Hoechst, Thermo Fisher Scientific) which stains chromatin blue
592 in all cells to count the total number of cells. 500 nM SYTOX and 10 uM Hoechst were directly
593 added into the dishes, and cells were incubated for 15 min. The fluorescent measurements
594 were using confocal microscopy. Hoechst and PI were excited by 405nm with the emission
595 between 405nm and 470nm. SYTOX was excited by a 488 nm laser with the emission between
596 488nm and 516nm. Percent cell death was quantified by the percent between the number of
597 red fluorescent cells in the total number of Hoechst 33342 expressing cells per image.

598

599 **Immunocytochemistry**

600 Cells were fixed in 4% paraformaldehyde and permeabilized with 0.2% Triton-X 100. 5% BSA
601 was used to block non-specific binding before cells were incubated with primary antibodies
602 either for 2 hours at room temperature or overnight at 4°C. The next day, cells were washed
603 three times with PBS and incubated with a secondary antibody for 1hr at room temperature.

604 Cells were mounted with an antifading medium after three times wash steps (DAPI was added
605 in the second wash if required) and let dry overnight.

606 Lists of primary antibodies used; Anti-GFAP antibody (abcam, ab7260, 1:500), Anti-beta III
607 Tubulin antibody (abcam, ab78078, 1:500). Lists of secondary antibodies used;Goat Anti-
608 Chicken IgY H&L (Alexa Fluor® 488) (abcam,ab150169, 1:500), GoatAnti-Mouse IgG H&L
609 (Alexa Fluor® 555) (abcam, ab150114, 1:500).

610 **Electrophysiology**

611 Patch-clamp recordings of iPSC-derived neurons were performed using an infrared
612 differential interference contrast (DIC) imaging system on an Olympus BX51WI upright
613 microscope (Olympus, Japan) coupled with a Multipatch 700B amplifier under the control of
614 pClamp 10.2 software package (Molecular Devices, USA), as described in detail previously.(*79*,
615 *80*) For the recordings, a neuronal culture or co-culture was plated on glass coverslips, placed
616 in a recording chamber mounted on the microscope stage and constantly perfused with a
617 physiological buffer medium. The perfusion medium contained (in mM) 126 NaCl, 2.5 KCl, 2
618 $MgSO_4$,2 $CaCl_2$, 26 $NaHCO_3$, 1.25 NaH_2PO4, 10 D-glucose and was continuously bubbled with
619 95% O_2 and 5% CO_2 (pH 7.4) and maintained at 30-33°C. Whole-cell recordings were
620 performed using glass pipettes with a resistance of 3.5-6 MΩ when filled with the intracellular
621 solution. This solution contained (in mM): 126 K-gluconate, 4 KCl, 4 $MgCl_2$, 2 BAPTA, 4 Mg-
622 ATP, 0.4 Na-ATP (pH 7.2, osmolarity ~295 mOsmol). In the whole-cell (immediately after
623 membrane breakthrough), iPSC-derived neurons were recorded for the resting membrane
624 potential (Vrest), membrane capacitance (Cm), the membrane time constant (τm), and input
625 resistance (Rin). To induce neuronal firing, a series of sub- and supra-threshold rectangular
626 current pulses were applied with a stepwise-increased stimulus intensity at the Vhold set at
627 −60 mV to −75 mV. The second protocol tested was a slow-ramp current injection, ramped up
628 with a 100–200 pA/s slope. The analysis of the AP waveform was performed for the first AP
629 only to quantify the threshold value, the spike amplitude, overshoot, the spike width
630 (duration at half-maximal amplitude), the rates of depolarisation and repolarisation phases
631 as previously described (*81*).

632

633 **Isolation of single cells**

634 Collecting cell pellets for bulk RNA-seq

635 To collect cell pellets, samples were trypsinised or scraped from the culture surface and
636 placed in a 15ml conical tube. These tubes were centrifuged at 800g in a refrigerated
637 centrifuge for 5 minutes, and the culture media decanted. The pellet was resuspended in 10ml
638 chilled PBS per tube by pipetting, then centrifuged again using the above parameters before
639 decanting the PBS. For bulk RNA sequencing, the cell pellets were frozen on dry ice and stored
640 at -80.

641 Collecting cell pellets for single cell RNA-seq

642 Samples for single cell RNA sequencing followed the procedure above, though instead of
643 freezing, the pellets were resuspended in 1ml PBS, and 100,000 cells were transferred to a
644 1.5ml falcon tube. These were centrifuged at 1000 rpm for 3 min at 4°C, before resuspending
645 cells in 20ul chilled DPS. 180ul chilled 100% methanol was added dropwise to the cells while
646 gently vortexing to prevent the cells from clumping, before fixing the cells on ice for 15 mins.

647

648 **Single-cell RNA-sequencing data generation and processing**

649 Between 2400 to 4000 cells were loaded for each sample into a separate channel of a
650 Chromium Chip G for use in the 10X Chromium Controller. The cells were partitioned into
651 nanoliter scale Gel Beads in emulsions (GEMs) and lysed using the 10x Genomics Single Cell
652 3' Chip V3.1 GEM, Library and Gel Bead Kit . cDNA synthesis and library construction were
653 performed as per the manufacturer's instructions. The RNA was reversed transcribed and
654 amplified using 12 cycles of PCR. Libraries were prepared from 10 µl of the cDNA and 13 cycles
655 of amplification. Each library was prepared using Single Index Kit T Set A and sequenced on
656 the HiSeq4000 system (Illumina) using 100 bp paired-end run at a mean depth of 20-50 million
657 reads per cell. Libraries were generated in independent runs for the different samples.

658 The reads were aligned to the human reference genome (Ensembl release 93, GRCh38) using
659 Cell Ranger v3.0.2. The analysis was carried out using Seurat v3.0(*82*, *83*) following Seurat's
660 standard workflow. Cells expressing fewer than 200 genes were excluded from the
661 subsequent analysis. In addition, we excluded cells with more than 3000 detected genes to

662 remove suspected cell doublets or multiplets. Given that certain cell types, e.g. neurons,
663 naturally express higher levels of mitochondrial genes, we applied a 10% cut-off for the
664 percentage of mitochondrial genes expressed to filter out likely apoptotic cells. Using default
665 parameters of Seurat, data for each sample were log normalised across cells and the 2000
666 most highly variable genes identified. Using the canonical correlation analysis ('CCA') (*83*) to
667 identify anchors, we integrated the samples using Seurat v3 (*82*, *83*), followed by regression
668 of the effect of cell cycle and scaling of the data. Dimensional reduction was performed using
669 50 PCs. We used Clustree v0.4.4 and Seurat's plot functions to visualise the expression of
670 astrocytic and neuronal marker genes across different cluster resolutions (0.05 - 0.5 in 0.05
671 increments and 0.5 - 1.0 in 0.1 increments) (*84*). A clustering resolution 0.25 was selected, as
672 it was the lowest resolution that explained the heterogeneity in the samples. The
673 differentially expressed genes between the clusters of interest were identified using Seurat's
674 FindMarkers() and the default 'Wilcox' test.

675

676 **Bulk tissue RNA-sequencing data generation and processing**

677 Libraries for sequencing were prepared using the Illumina TruSeq Stranded mRNA Library
678 Prep kit by loading 50 ng of total RNA into the initial reaction; fragmentation and PCR steps
679 were undertaken as per the manufacturer's instructions. Final library concentrations were
680 determined using Qubit 2.0 fluorometer and pooled to a normalized input library. Pools were
681 sequenced using the Illumina NovaSeq 6000 Sequencing system to generate 150 bp paired-
682 end reads with an average read depth of ~137 million paired-end reads per sample.

683 We performed pre-alignment quality control using Fastp (v 0.20.0) with default settings, for
684 adapter trimming, read filtering and base correction (*85*). Processed reads were aligned to
685 the GRCh38 human reference genome using 2-pass STAR (v 2.7.0a), with gene annotations
686 from Ensembl v93 (*86*, *87*). Parameters were set to match ENCODE options except, we only
687 retained uniquely mapped reads and used STAR's default of a minimum 3 bp overhang
688 required for an annotated spliced alignment. Post-alignment quality metrics were generated
689 using RSeQC (v2.6.4) and MultiQC (v1.8.dev0) (*88*, *89*). We found that an average of 90.4%
690 reads were uniquely mapped.

691 The processed reads were also quantified with Salmon (v 0.14.1) using the mapping-based
692 mode with a decoy-aware transcriptome based on GRCh38 and Ensembl v93 as the reference
693 (*90*). Salmon's options correcting for sequence, non-uniform coverage biases (including 5' or
694 3' bias) and GC bias in the data were enabled and the R package tximport used to transform
695 Salmon transcript-level abundance estimates to gene-level values (*91*). Pipeline source code
696 can be found in https://github.com/RHReynolds/RNAseqProcessing.

697 **Deconvolution**

698 Cell type proportions in the bulk tissue RNA-sequencing samples were estimated using Scaden
699 (v1.1.2) (*34*). Scaden trains on simulated bulk RNA-sequencing samples, generated from
700 tissue-specific single cell data, and predicts cell type proportions in bulk tissue RNA-
701 sequencing data. The training data was generated using the raw counts and cell types based
702 on the clustering 0.25 from the single cell data. Thereby we created 2,000 artificial bulk tissue
703 RNA-sequencing samples by randomly selecting 3,000 cells from the total of 8,132 cells.
704 Prediction of the cell type proportions were made using the default parameters and the
705 Scaden developers' recommendations. Following deconvolution, significant differences in the
706 cell type proportions between the αsyn-O treated and basal astrocytes and co-culture were
707 investigated using a paired t-test and multiple comparison correction using Benjamini &
708 Hochberg method, per cell culture. This was only applied to cell types with proportions >=
709 0.01, which included Astrocyte clusters 1 and 2 and Neuron clusters 1, 2 and 3.

710 **Differential gene expression analysis**

711 Sources of variation in bulk tissue RNA-sequencing data were assessed by performing
712 principal component analysis on the gene level expression filtered to include genes expressed
713 in all samples of each cell culture and treatment.

714 We found that cell culture and cell-type proportions were significantly correlated with the
715 first PC (**Supp fig. 3b**). The individual, age and sex correlated with PC2. Individual, RIN and
716 astrocyte cluster 2 correlated with PC3, while culture, individual, age and neuron cluster 5
717 were significantly correlated with PC4. The treatment applied to the cell culture correlated
718 with PC5. Accordingly, PC axes 2, 3 and 4 were included as covariates in the model for
719 differential expression and splicing analyses of the bulk-tissue RNA-sequencing data. Bulk-
720 tissue differential gene expression was examined using DESeq2 (v1.30.1) (*92*), including only

721 genes expressed in all samples within a cell culture and treatment group, collapsing across
722 individuals in a cell culture and treatment group; and controlling for covariates. A cut-off of
723 FDR < 5% was used to consider a gene as significantly differentially expressed.

724

725 **Differential splicing analysis**

726 Differential splicing analysis was conducted using Leafcutter (v0.2.9) (*93*). It detects changes
727 in alternative splicing events by constructing clusters of introns that share splice sites and
728 determining the difference in intron usage, measuring differential splicing in terms of the
729 change in the percent spliced in (ΔPSI). Splice junctions outputted by STAR were filtered to
730 remove those with length < 25 nucleotides and regions that overlapped the ENCODE blacklist
731 regions (https://github.com/Boyle-Lab/Blacklist/tree/master/lists) (*94*). The junctions were
732 annotated using junction_annot() from dasper (*95*), classifying them into the following
733 categories, (based on if one end (acceptor or donor) or both ends match the boundary of a
734 known exon) - annotated, novel acceptor, novel donor, novel combination, novel exon skip,
735 unannotated and ambiguous gene (mapped to more than 1 gene). Those annotated as
736 ambiguous were excluded from this analysis. Leafcutter was run to identify intron clusters by
737 excluding introns of length greater than 1 Mb and those that were supported by < 30 junction
738 reads across all the samples or < 0.1% of the total number of junction read counts for the
739 entire cluster. Differentially spliced clusters were identified pairwise, in treated vs untreated
740 astrocytes and co-culture samples, using leafcutter's default parameters and controlling for
741 covariates as identified by the gene level expression. 40,892 and 44,390 clusters (that lie in a
742 single gene) were successfully tested for differential splicing in the astrocytes treated vs
743 untreated and co-culture treated vs untreated respectively. An intron cluster and its
744 overlapping gene were considered differentially spliced at FDR < 0.05 if the intron cluster
745 contained at least one intron with an absolute delta percent spliced-in value (|ΔPSI|) ≥ 0.1.
746 Functional enrichment analysis was performed using clusterProfiler (v3.18.1).(*96*) Gene
747 ontology over-representation analyses were run and comparisons between genelists made
748 using compareCluster(). We analysed differentially expressed genes at FDR < 5% and with at
749 least >= 2 fold change in expression and differentially spliced genes at FDR < 5% and |ΔPSI|
750 ≥ 0.1 .

751 ADAR's differentially spliced transcripts were linked to the protein isoforms by first identifying
752 the transcripts the differentially spliced junctions overlapped with. The junctions overlapped
753 with transcripts ADAR-201 and ADAR-202. The number of amino acids in these transcripts
754 matched to P55265-5 (synonym p110) and P55265-1 (synonym p150) in Uniprot (*97*)
755 respectively. We further ran multiple sequence alignment of the amino acid sequences from
756 UniProt and Ensembl (obtained from the in silico translated mRNA is translated) for each of
757 the isoforms, that was a match. ADAR's differentially spliced junctions were visualised with
758 ADAR's protein coding transcript structures using ggtranscript (*98*).

759

760 **A-to-I editing**

761 RNA editing analysis was undertaken with JACUSA2 v2.0.2 (https://github.com/dieterich-
762 lab/JACUSA2), leveraging GNU parallel v20230722 (https://www.gnu.org/software/parallel/)
763 (*99–101*). This utilises a drichilet multinomial distribution to ascertain whether transcripts are
764 edited at a genomic site in two modes: in 'detect' mode it compares transcripts against a
765 reference genome identifying editing in individual samples; in 'differential' mode it will
766 compare two samples against each other, looking at sites that are differentially edited in one
767 sample compared to another. Noting that transcripts with increased editing might not be
768 successfully mapped during the alignment step, multi-sample 2-pass mapping with STAR
769 v2.7.9a (https://code.google.com/archive/p/rna-star/) was re-run, allowing a more generous
770 mismatch rate of 16 base pairs per 100.(*86*) This did not increase the rate of multimapping
771 during alignment**.** PCR duplicates were identified by samtools v1.13 markdup
772 (https://www.htslib.org) (*102*). A-to-I editing was assessed in properly paired, non-duplicate
773 reads, with settings to exclude any potential editing sites near the start and end of reads,
774 indel positions and splice sites, as well as sites within homopolymer runs of more than 7 bases.
775 An editing site was considered significant if it had an absolute z score greater than 1.96 ($|z|$
776 ≥ 1.96). Replicates for each sample group were input to JACUSA2 detect to output a list of
777 editing sites for each of the six groups: astrocytes untreated, astrocytes treated, co-culture
778 untreated, co-culture treated, neuron untreated and neuron treated. Differences in editing
779 sites and rates were explored using R (v 4.2, www.r-project.org). JACUSA2 differential was
780 used to ascertain those sites that were differentially edited in treated samples of each cell
781 line, compared to untreated. Edits were annotated with Ensembl's variant effect predictor

782 (VEP, v93.5, https://www.ensembl.org/info/docs/tools/vep), filtering duplicate results by
783 consequence, and biotypes of interest (*103*). Where results were not derived with Ensembl
784 VEP, a manual annotation was undertaken using the Ensembl GTF file, deriving genic location
785 and biotype. Editing sites were also annotated with repeat motifs downloaded from
786 RepeatMasker v4.0.5 (http://www.repeatmasker.org/) (*104*). Functional enrichment of the
787 differentially edited genes (FDR< 5%) that were also differentially expressed (FDR< 5% & at
788 least 2 fold change in expression) was examined using clusterprofiler (v3.18.1) (*96*).

789 **Post-mortem brain editing analysis**

790 Post-mortem human brain samples were sourced from publicly available data, including bulk
791 and single-nuclear RNA sequencing data from 5 control and 7 PD anterior cingulate cortex
792 samples from donors with Braak stage 5-6 disease (*105*). Single-nuclear gene expression was
793 explored in python 3.9 (www.python.org) using the pl.dotplot function from scanpy 1.7.2
794 (*106*). As with the cellular models, bulk transcriptomic samples were passed through the
795 editing pipeline including trimming with fastp, and alignment with STAR allowing 16 base
796 mismatches per 100, and then identification of editing sites using JACUSA2 as above. Using R
797 4.2.0, sites were filtered to include those present in at least 2 samples per PD and control
798 group, and presence in both groups. Sites with editing rate greater than 0 and less than 1
799 were input into a linear regression as follows: Editing_rate ~ Disease_Group + Sex + RIN.
800 Expression weighted celltype enrichment (EWCE v1.11.3,
801 nathanskene.github.io/EWCE/index.html) analysis was undertaken using specificity matrices
802 previously derived for this dataset from single nuclear RNA sequencing results (*59*, *105*). The
803 ranked gene list input to EWCE was defined by the genes with the greatest increase in mean
804 editing rate, relative to all the genes where editing was detected including genes with editing
805 rate of 1.

806

807 # References

808

809 1. H. Braak, K. Del Tredici, U. Rüb, R. A. I. de Vos, E. N. H. Jansen Steur, E. Braak, Staging
810 of brain pathology related to sporadic Parkinson's disease. *Neurobiol. Aging* **24**, 197–
811 211 (2003).

812 2. P. Damier, E. C. Hirsch, P. Zhang, Y. Agid, F. Javoy-Agid, Glutathione peroxidase, glial
813 cells and Parkinson's disease. *Neuroscience* **52**, 1–6 (1993).

814 3. C. Knott, G. P. Wilkin, G. Stern, Astrocytes and microglia in the substantia nigra and
815 caudate-putamen in Parkinson's disease. *Parkinsonism Relat. Disord.* **5**, 115–122
816 (1999).

817 4. D.-K. Choi, S. Pennathur, C. Perier, K. Tieu, P. Teismann, D.-C. Wu, V. Jackson-Lewis, M.
818 Vila, J.-P. Vonsattel, J. W. Heinecke, S. Przedborski, Ablation of the Inflammatory
819 Enzyme Myeloperoxidase Mitigates Features of Parkinson's Disease in Mice. *J.*
820 *Neurosci.* **25**, 6594–6600 (2005).

821 5. J. Miklossy, D. D. Doudet, C. Schwab, S. Yu, E. G. McGeer, P. L. McGeer, Role of ICAM-1
822 in persisting inflammation in Parkinson disease and MPTP monkeys. *Exp. Neurol.* **197**,
823 275–283 (2006).

824 6. I. Lastres-Becker, A. Ulusoy, N. G. Innamorato, G. Sahin, A. Rábano, D. Kirik, A.
825 Cuadrado, α-Synuclein expression and Nrf2 deficiency cooperate to aggravate protein
826 aggregation, neuronal death and inflammation in early-stage Parkinson's disease. *Hum.*
827 *Mol. Genet.* **21**, 3173–3192 (2012).

828 7. K. Sathe, W. Maetzler, J. D. Lang, R. B. Mounsey, C. Fleckenstein, H. L. Martin, C. Schulte,
829 S. Mustafa, M. Synofzik, Z. Vukovic, S. Itohara, D. Berg, P. Teismann, S100B is increased
830 in Parkinson's disease and ablation protects against MPTP-induced toxicity through the
831 RAGE and TNF-α pathway. *Brain* **135**, 3336–3347 (2012).

832 8. Z. A. Sorrentino, Y. Xia, C. Funk, C. J. Riffe, N. J. Rutherford, C. Ceballos Diaz, A. N. Sacino,
833 N. D. Price, T. E. Golde, B. I. Giasson, P. Chakrabarty, Motor neuron loss and
834 neuroinflammation in a model of α-synuclein-induced neurodegeneration. *Neurobiol.*
835 *Dis.* **120**, 98–106 (2018).

836 9. A. J. Schaser, T. L. Stackhouse, L. J. Weston, P. C. Kerstein, V. R. Osterberg, C. S. López,
837 D. W. Dickson, K. C. Luk, C. K. Meshul, R. L. Woltjer, V. K. Unni, Trans-synaptic and
838 retrograde axonal spread of Lewy pathology following pre-formed fibril injection in an
839 in vivo A53T alpha-synuclein mouse model of synucleinopathy. *Acta Neuropathol.*
840 *Commun.* **8**, 150 (2020).

841 10. M. F. Altay, A. K. L. Liu, J. L. Holton, L. Parkkinen, H. A. Lashuel, Prominent astrocytic
842 alpha-synuclein pathology with unique post-translational modification signatures
843 unveiled across Lewy body disorders. *Acta Neuropathol. Commun.* **10**, 163 (2022).

844 11. F. Weiss, A. Labrador-Garrido, N. Dzamko, G. Halliday, Immune responses in the
845 Parkinson's disease brain. *Neurobiol. Dis.* **168**, 105700 (2022).

846 12. H.-G. Lee, M. A. Wheeler, F. J. Quintana, Function and therapeutic value of astrocytes
847 in neurological diseases. *Nat. Rev. Drug Discov.* **21**, 339–358 (2022).

848 13. S. A. Liddelow, K. A. Guttenplan, L. E. Clarke, F. C. Bennett, C. J. Bohlen, L. Schirmer, M.
849 L. Bennett, A. E. Münch, W.-S. Chung, T. C. Peterson, D. K. Wilton, A. Frouin, B. A.

850 Napier, N. Panicker, M. Kumar, M. S. Buckwalter, D. H. Rowitch, V. L. Dawson, T. M.
851 Dawson, B. Stevens, B. A. Barres, Neurotoxic reactive astrocytes are induced by
852 activated microglia. *Nature* **541**, 481–487 (2017).

853 14. L. Barbar, T. Jain, M. Zimmer, I. Kruglikov, J. S. Sadick, M. Wang, K. Kalpana, I. V. L. Rose,
854 S. R. Burstein, T. Rusielewicz, M. Nijsure, K. A. Guttenplan, A. di Domenico, G. Croft, B.
855 Zhang, H. Nobuta, J. M. Hébert, S. A. Liddelow, V. Fossati, CD49f Is a Novel Marker of
856 Functional and Reactive Human iPSC-Derived Astrocytes. *Neuron* **107**, 436-453.e12
857 (2020).

858 15. J. S. Sadick, M. R. O'Dea, P. Hasel, T. Dykstra, A. Faustin, S. A. Liddelow, Astrocytes and
859 oligodendrocytes undergo subtype-specific transcriptional changes in Alzheimer's
860 disease. *Neuron* **110**, 1788-1805.e10 (2022).

861 16. E. Shigetomi, S. Patel, B. S. Khakh, Probing the Complexities of Astrocyte Calcium
862 Signaling. *Trends Cell Biol.* **26**, 300–312 (2016).

863 17. C. Escartin, E. Galea, A. Lakatos, J. P. O'Callaghan, G. C. Petzold, A. Serrano-Pozo, C.
864 Steinhäuser, A. Volterra, G. Carmignoto, A. Agarwal, N. J. Allen, A. Araque, L. Barbeito,
865 A. Barzilai, D. E. Bergles, G. Bonvento, A. M. Butt, W.-T. Chen, M. Cohen-Salmon, C.
866 Cunningham, B. Deneen, B. De Strooper, B. Díaz-Castro, C. Farina, M. Freeman, V. Gallo,
867 J. E. Goldman, S. A. Goldman, M. Götz, A. Gutiérrez, P. G. Haydon, D. H. Heiland, E. M.
868 Hol, M. G. Holt, M. Iino, K. V. Kastanenka, H. Kettenmann, B. S. Khakh, S. Koizumi, C. J.
869 Lee, S. A. Liddelow, B. A. MacVicar, P. Magistretti, A. Messing, A. Mishra, A. V. Molofsky,
870 K. K. Murai, C. M. Norris, S. Okada, S. H. R. Oliet, J. F. Oliveira, A. Panatier, V. Parpura,
871 M. Pekna, M. Pekny, L. Pellerin, G. Perea, B. G. Pérez-Nievas, F. W. Pfrieger, K. E.
872 Poskanzer, F. J. Quintana, R. M. Ransohoff, M. Riquelme-Perez, S. Robel, C. R. Rose, J.
873 D. Rothstein, N. Rouach, D. H. Rowitch, A. Semyanov, S. Sirko, H. Sontheimer, R. A.
874 Swanson, J. Vitorica, I.-B. Wanner, L. B. Wood, J. Wu, B. Zheng, E. R. Zimmer, R. Zorec,
875 M. V. Sofroniew, A. Verkhratsky, Reactive astrocyte nomenclature, definitions, and
876 future directions. *Nat. Neurosci.* **24**, 312–325 (2021).

877 18. C. D. Hughes, M. L. Choi, M. Ryten, L. Hopkins, A. Drews, J. A. Botía, M. Iljina, M.
878 Rodrigues, S. A. Gagliano, S. Gandhi, C. Bryant, D. Klenerman, Picomolar concentrations
879 of oligomeric alpha-synuclein sensitizes TLR4 to play an initiating role in Parkinson's
880 disease pathogenesis. *Acta Neuropathol. (Berl.)* **137**, 103–120 (2019).

881 19. S. P. Yun, T.-I. Kam, N. Panicker, S. Kim, Y. Oh, J.-S. Park, S.-H. Kwon, Y. J. Park, S. S.
882 Karuppagounder, H. Park, S. Kim, N. Oh, N. A. Kim, S. Lee, S. Brahmachari, X. Mao, J. H.
883 Lee, M. Kumar, D. An, S.-U. Kang, Y. Lee, K. C. Lee, D. H. Na, D. Kim, S. H. Lee, V. V.
884 Roschke, S. A. Liddelow, Z. Mari, B. A. Barres, V. L. Dawson, S. Lee, T. M. Dawson, H. S.
885 Ko, Block of A1 astrocyte conversion by microglia is neuroprotective in models of
886 Parkinson's disease. *Nat. Med.* **24**, 931–938 (2018).

887 20. P. Hasel, I. V. L. Rose, J. S. Sadick, R. D. Kim, S. A. Liddelow, Neuroinflammatory
888 astrocyte subtypes in the mouse brain. *Nat. Neurosci.* **24**, 1475–1487 (2021).

889 21. K. Russ, G. Teku, L. Bousset, V. Redeker, S. Piel, E. Savchenko, Y. Pomeshchik, J.
890 Savistchenko, T. C. Stummann, C. Azevedo, A. Collin, S. Goldwurm, K. Fog, E. Elmer, M.

891 Vihinen, R. Melki, L. Roybon, TNF-α and α-synuclein fibrils differently regulate human
892 astrocyte immune reactivity and impair mitochondrial respiration. *Cell Rep.* **34**, 108895
893 (2021).

894 22. J. Rostami, G. Fotaki, J. Sirois, R. Mzezewa, J. Bergström, M. Essand, L. Healy, A.
895 Erlandsson, Astrocytes have the capacity to act as antigen-presenting cells in the
896 Parkinson's disease brain. *J. Neuroinflammation* **17**, 119 (2020).

897 23. N. Bengoa-Vergniory, R. F. Roberts, R. Wade-Martins, J. Alegre-Abarrategui, Alpha-
898 synuclein oligomers: a new hope. *Acta Neuropathol. (Berl.)* **134**, 819–838 (2017).

899 24. P. R. Angelova, M. L. Choi, A. V. Berezhnov, M. H. Horrocks, C. D. Hughes, S. De, M.
900 Rodrigues, R. Yapom, D. Little, K. S. Dolt, T. Kunath, M. J. Devine, P. Gissen, M. S.
901 Shchepinov, S. Sylantyev, E. V. Pavlov, D. Klenerman, A. Y. Abramov, S. Gandhi, Alpha
902 synuclein aggregation drives ferroptosis: an interplay of iron, calcium and lipid
903 peroxidation. *Cell Death Differ.* **27**, 2781–2796 (2020).

904 25. M. L. Choi, A. Chappard, B. P. Singh, C. Maclachlan, M. Rodrigues, E. I. Fedotova, A. V.
905 Berezhnov, S. De, C. J. Peddie, D. Athauda, G. S. Virdi, W. Zhang, J. R. Evans, A. I.
906 Wernick, Z. S. Zanjani, P. R. Angelova, N. Esteras, A. Y. Vinokurov, K. Morris, K. Jeacock,
907 L. Tosatto, D. Little, P. Gissen, D. J. Clarke, T. Kunath, L. Collinson, D. Klenerman, A. Y.
908 Abramov, M. H. Horrocks, S. Gandhi, Pathological structural conversion of α-synuclein
909 at the mitochondria induces neuronal toxicity. *Nat. Neurosci.* **25**, 1134–1148 (2022).

910 26. E. Deas, N. Cremades, P. R. Angelova, M. H. R. Ludtmann, Z. Yao, S. Chen, M. H.
911 Horrocks, B. Banushi, D. Little, M. J. Devine, P. Gissen, D. Klenerman, C. M. Dobson, N.
912 W. Wood, S. Gandhi, A. Y. Abramov, Alpha-Synuclein Oligomers Interact with Metal
913 Ions to Induce Oxidative Stress and Neuronal Death in Parkinson's Disease. *Antioxid.*
914 *Redox Signal.* **24**, 376–391 (2016).

915 27. K. Leng, I. V. L. Rose, H. Kim, W. Xia, W. Romero-Fernandez, B. Rooney, M. Koontz, E.
916 Li, Y. Ao, S. Wang, M. Krawczyk, J. Tcw, A. Goate, Y. Zhang, E. M. Ullian, M. V. Sofroniew,
917 S. P. J. Fancy, M. S. Schrag, E. S. Lippmann, M. Kampmann, CRISPRi screens in human
918 iPSC-derived astrocytes elucidate regulators of distinct inflammatory reactive states.
919 *Nat. Neurosci.* **25**, 1528–1542 (2022).

920 28. B. E. Clarke, D. M. Taha, O. J. Ziff, A. Alam, E. P. Thelin, N. M. García, A. Helmy, R. Patani,
921 Human stem cell-derived astrocytes exhibit region-specific heterogeneity in their
922 secretory profiles. *Brain* **143**, e85 (2020).

923 29. C. E. Hall, Z. Yao, M. Choi, G. E. Tyzack, A. Serio, R. Luisier, J. Harley, E. Preza, C. Arber,
924 S. J. Crisp, P. M. D. Watson, D. M. Kullmann, A. Y. Abramov, S. Wray, R. Burley, S. H. Y.
925 Loh, L. M. Martins, M. M. Stevens, N. M. Luscombe, C. R. Sibley, A. Lakatos, J. Ule, S.
926 Gandhi, R. Patani, Progressive Motor Neuron Pathology and the Role of Astrocytes in a
927 Human Stem Cell Model of VCP-Related ALS. *Cell Rep.* **19**, 1739–1749 (2017).

928 30. M. H. R. Ludtmann, P. R. Angelova, M. H. Horrocks, M. L. Choi, M. Rodrigues, A. Y. Baev,
929 A. V. Berezhnov, Z. Yao, D. Little, B. Banushi, A. S. Al-Menhali, R. T. Ranasinghe, D. R.
930 Whiten, R. Yapom, K. S. Dolt, M. J. Devine, P. Gissen, T. Kunath, M. Jaganjac, E. V. Pavlov,

931 D. Klenerman, A. Y. Abramov, S. Gandhi, α-synuclein oligomers interact with ATP
932 synthase and open the permeability transition pore in Parkinson's disease. *Nat.*
933 *Commun.* **9**, 2293 (2018).

934 31. D. Wang, S. Liu, J. Warrell, H. Won, X. Shi, F. C. P. Navarro, D. Clarke, M. Gu, P. Emani,
935 Y. T. Yang, M. Xu, M. J. Gandal, S. Lou, J. Zhang, J. J. Park, C. Yan, S. K. Rhie, K.
936 Manakongtreecheep, H. Zhou, A. Nathan, M. Peters, E. Mattei, D. Fitzgerald, T.
937 Brunetti, J. Moore, Y. Jiang, K. Girdhar, G. E. Hoffman, S. Kalayci, Z. H. Gümüş, G. E.
938 Crawford, PsychENCODE Consortium, P. Roussos, S. Akbarian, A. E. Jaffe, K. P. White, Z.
939 Weng, N. Sestan, D. H. Geschwind, J. A. Knowles, M. B. Gerstein, Comprehensive
940 functional genomic resource and integrative model for the human brain. *Science* **362**
941 (2018).

942 32. A. Zeisel, A. B. Muñoz-Manchado, S. Codeluppi, P. Lönnerberg, G. La Manno, A. Juréus,
943 S. Marques, H. Munguba, L. He, C. Betsholtz, C. Rolny, G. Castelo-Branco, J. Hjerling-
944 Leffler, S. Linnarsson, Cell types in the mouse cortex and hippocampus revealed by
945 single-cell RNA-seq. *Science* **347**, 1138–1142 (2015).

946 33. Measuring reactive species and oxidative damage in vivo and in cell culture: how should
947 you do it and what do the results mean? - Halliwell - 2004 - British Journal of
948 Pharmacology - Wiley Online Library.
949 https://bpspubs.onlinelibrary.wiley.com/doi/full/10.1038/sj.bjp.0705776.

950 34. K. Menden, M. Marouf, S. Oller, A. Dalmia, D. S. Magruder, K. Kloiber, P. Heutink, S.
951 Bonn, Deep learning–based cell composition analysis from tissue expression profiles.
952 *Sci. Adv.* **6**, eaba2619 (2020).

953 35. A. G. L. Douglas, M. J. A. Wood, RNA splicing: disease and therapy. *Brief. Funct.*
954 *Genomics* **10**, 151–164 (2011).

955 36. M. M. Scotti, M. S. Swanson, RNA mis-splicing in disease. *Nat. Rev. Genet.* **17**, 19–32
956 (2016).

957 37. S. García-Ruiz, E. K. Gustavsson, D. Zhang, R. H. Reynolds, Z. Chen, A. Fairbrother-
958 Browne, A. L. Gil-Martínez, J. A. Botia, L. Collado-Torres, M. Ryten, IntroVerse: a
959 comprehensive database of introns across human tissues. *Nucleic Acids Res.* **51**, D167–
960 D178 (2023).

961 38. M. J. Raymond, P. Ray, G. Kaur, M. Fredericks, A. V. Singh, L. Q. Wan, Multiaxial Polarity
962 Determines Individual Cellular and Nuclear Chirality. *Cell. Mol. Bioeng.* **10**, 63–74
963 (2017).

964 39. Z. Zhang, K. C. M. Lee, D. M. D. Siu, M. C. K. Lo, Q. T. K. Lai, E. Y. Lam, K. K. Tsia,
965 Morphological profiling by high-throughput single-cell biophysical fractometry.
966 *Commun. Biol.* **6**, 1–13 (2023).

967 40. A. R. Martin, E. Williams, R. E. Foulger, S. Leigh, L. C. Daugherty, O. Niblock, I. U. S.
968 Leong, K. R. Smith, O. Gerasimenko, E. Haraldsdottir, E. Thomas, R. H. Scott, E. Baple,
969 A. Tucci, H. Brittain, A. de Burca, K. Ibañez, D. Kasperaviciute, D. Smedley, M. Caulfield,

970 A. Rendon, E. M. McDonagh, PanelApp crowdsources expert knowledge to establish
971 consensus diagnostic gene panels. *Nat. Genet.* **51**, 1560–1565 (2019).

972 41. M. A. Nalls, C. Blauwendraat, C. L. Vallerga, K. Heilbron, S. Bandres-Ciga, D. Chang, M.
973 Tan, D. A. Kia, A. J. Noyce, A. Xue, J. Bras, E. Young, R. von Coelln, J. Simón-Sánchez, C.
974 Schulte, M. Sharma, L. Krohn, L. Pihlstrøm, A. Siitonen, H. Iwaki, H. Leonard, F. Faghri,
975 J. R. Gibbs, D. G. Hernandez, S. W. Scholz, J. A. Botia, M. Martinez, J.-C. Corvol, S. Lesage,
976 J. Jankovic, L. M. Shulman, M. Sutherland, P. Tienari, K. Majamaa, M. Toft, O. A.
977 Andreassen, T. Bangale, A. Brice, J. Yang, Z. Gan-Or, T. Gasser, P. Heutink, J. M. Shulman,
978 N. W. Wood, D. A. Hinds, J. A. Hardy, H. R. Morris, J. Gratten, P. M. Visscher, R. R.
979 Graham, A. B. Singleton, 23andMe Research Team, System Genomics of Parkinson's
980 Disease Consortium, International Parkinson's Disease Genomics Consortium,
981 Identification of novel risk loci, causal insights, and heritable risk for Parkinson's
982 disease: a meta-analysis of genome-wide association studies. *Lancet Neurol.* **18**, 1091–
983 1102 (2019).

984 42. J. Quin, J. Sedmík, D. Vukić, A. Khan, L. P. Keegan, M. A. O'Connell, ADAR RNA
985 Modifications, the Epitranscriptome and Innate Immunity. *Trends Biochem. Sci.* **46**,
986 758–771 (2021).

987 43. Y. G. Chen, S. Hur, Cellular origins of dsRNA, their recognition and consequences. *Nat.*
988 *Rev. Mol. Cell Biol.* **23**, 286–301 (2022).

989 44. Y. Hao, B. Yang, J. Yang, X. Shi, X. Yang, D. Zhang, D. Zhao, W. Yan, L. Chen, H. Zheng, K.
990 Zhang, X. Liu, ZBP1: A Powerful Innate Immune Sensor and Double-Edged Sword in Host
991 Immunity. *Int. J. Mol. Sci.* **23**, 10224 (2022).

992 45. K. Nishikura, Functions and regulation of RNA editing by ADAR deaminases. *Annu. Rev.*
993 *Biochem.* **79**, 321–349 (2010).

994 46. K. A. Cottrell, R. J. Andrews, B. L. Bass, The competitive landscape of the dsRNA world.
995 *Mol. Cell* **84**, 107–119 (2024).

996 47. K. Sinigaglia, A. Cherian, D. Vukic, J. Melicherova, P. Linhartova, Q. Du, L. Zerad, S.
997 Stejskal, R. Malik, J. Prochazka, N. Bondurand, R. Sedlacek, M. A. O'Connell, L. P.
998 Keegan, "Aberrant activation of the innate immune sensor PKR by self dsRNA is
999 prevented by direct interaction with ADAR1" (preprint, Immunology, 2023);
1000 https://doi.org/10.1101/2023.08.29.555105.

1001 48. S. Zhou, C. Yang, F. Zhao, Y. Huang, Y. Lin, C. Huang, X. Ma, J. Du, Y. Wang, G. Long, J.
1002 He, C. Liu, P. Zhang, Double-stranded RNA deaminase ADAR1 promotes the Zika virus
1003 replication by inhibiting the activation of protein kinase PKR. *J. Biol. Chem.* **294**, 18168–
1004 18180 (2019).

1005 49. A. D. J. Scadden, Inosine-containing dsRNA binds a stress-granule-like complex and
1006 downregulates gene expression in trans. *Mol. Cell* **28**, 491–500 (2007).

1007 50. Y. J. Crow, N. Manel, Aicardi–Goutières syndrome and the type I interferonopathies.
1008 *Nat. Rev. Immunol.* **15**, 429–440 (2015).

1009 51. A. Gallo, D. Vukic, D. Michalík, M. A. O'Connell, L. P. Keegan, ADAR RNA editing in
1010 human disease; more to it than meets the I. *Hum. Genet.* **136**, 1265–1278 (2017).

1011 52. W. H. Cuddleston, J. Li, X. Fan, A. Kozenkov, M. Lalli, S. Khalique, S. Dracheva, E. A.
1012 Mukamel, M. S. Breen, Cellular and genetic drivers of RNA editing variation in the
1013 human brain. *Nat. Commun.* **13**, 2997 (2022).

1014 53. I. X. Wang, E. So, J. L. Devlin, Y. Zhao, M. Wu, V. G. Cheung, ADAR regulates RNA editing,
1015 transcript stability, and gene expression. *Cell Rep.* **5**, 849–860 (2013).

1016 54. K. Hajji, J. Sedmík, A. Cherian, D. Amoruso, L. P. Keegan, M. A. O'Connell, ADAR2
1017 enzymes: efficient site-specific RNA editors with gene therapy aspirations. *RNA N. Y.*
1018 **28**, 1281–1297 (2022).

1019 55. L. A. O'Leary, M. A. Davoli, C. Belliveau, A. Tanti, J. C. Ma, W. T. Farmer, G. Turecki, K.
1020 K. Murai, N. Mechawar, Characterization of Vimentin-Immunoreactive Astrocytes in
1021 the Human Brain. *Front. Neuroanat.* **14** (2020).

1022 56. F. Cruz-Mendoza, F. Jauregui-Huerta, A. Aguilar-Delgadillo, J. García-Estrada, S. Luquin,
1023 Immediate Early Gene c-fos in the Brain: Focus on Glial Cells. *Brain Sci.* **12**, 687 (2022).

1024 57. E. K. Erickson, A. J. DaCosta, S. C. Mason, Y. A. Blednov, R. D. Mayfield, R. A. Harris,
1025 Cortical astrocytes regulate ethanol consumption and intoxication in mice.
1026 *Neuropsychopharmacology* **46**, 500–508 (2021).

1027 58. R. Feleke, R. H. Reynolds, A. M. Smith, B. Tilley, S. A. G. Taliun, J. Hardy, P. M. Matthews,
1028 S. Gentleman, D. R. Owen, M. R. Johnson, P. K. Srivastava, M. Ryten, Cross-platform
1029 transcriptional profiling identifies common and distinct molecular pathologies in Lewy
1030 body diseases. *Acta Neuropathol. (Berl.)* **142**, 449–474 (2021).

1031 59. N. G. Skene, S. G. N. Grant, Identification of Vulnerable Cell Types in Major Brain
1032 Disorders Using Single Cell Transcriptomes and Expression Weighted Cell Type
1033 Enrichment. *Front. Neurosci.* **10** (2016).

1034 60. M. V. Sofroniew, Astrocyte reactivity: subtypes, states, and functions in CNS innate
1035 immunity. *Trends Immunol.* **41**, 758–770 (2020).

1036 61. J. Mertens, D. Reid, S. Lau, Y. Kim, F. H. Gage, Aging in a Dish: iPSC-Derived and Directly
1037 Induced Neurons for Studying Brain Aging and Age-Related Neurodegenerative
1038 Diseases. *Annu. Rev. Genet.* **52**, 271–293 (2018).

1039 62. C. Farina, F. Aloisi, E. Meinl, Astrocytes are active players in cerebral innate immunity.
1040 *Trends Immunol.* **28**, 138–145 (2007).

1041 63. J. L. Zamanian, L. Xu, L. C. Foo, N. Nouri, L. Zhou, R. G. Giffard, B. A. Barres, Genomic
1042 analysis of reactive astrogliosis. *J. Neurosci.* **32**, 6391–6410 (2012).

1043 64. A. Soung, R. S. Klein, Viral Encephalitis and Neurologic Diseases: Focus on Astrocytes.
1044 *Trends Mol. Med.* **24**, 950–962 (2018).

1045 65. H.-J. Lee, J.-E. Suk, C. Patrick, E.-J. Bae, J.-H. Cho, S. Rho, D. Hwang, E. Masliah, S.-J. Lee,
1046 Direct Transfer of α-Synuclein from Neuron to Astroglia Causes Inflammatory
1047 Responses in Synucleinopathies *. *J. Biol. Chem.* **285**, 9262–9272 (2010).

1048 66. F. Cavaliere, L. Cerf, B. Dehay, P. Ramos-Gonzalez, F. De Giorgi, M. Bourdenx, A.
1049 Bessede, J. A. Obeso, C. Matute, F. Ichas, E. Bezard, In vitro α-synuclein neurotoxicity
1050 and spreading among neurons and astrocytes using Lewy body extracts from Parkinson
1051 disease brains. *Neurobiol. Dis.* **103**, 101–112 (2017).

1052 67. A. Filippini, V. Mutti, G. Faustini, F. Longhena, I. Ramazzina, F. Rizzi, A. Kaganovich, D.
1053 A. Roosen, N. Landeck, M. Duffy, I. Tessari, F. Bono, C. Fiorentini, E. Greggio, L. Bubacco,
1054 A. Bellucci, M. Missale, M. R. Cookson, M. Gennarelli, I. Russo, Extracellular clusterin
1055 limits the uptake of α-synuclein fibrils by murine and human astrocytes. *Glia* **69**, 681–
1056 696 (2021).

1057 68. J. Rostami, S. Holmqvist, V. Lindström, J. Sigvardson, G. T. Westermark, M. Ingelsson, J.
1058 Bergström, L. Roybon, A. Erlandsson, Human Astrocytes Transfer Aggregated Alpha-
1059 Synuclein via Tunneling Nanotubes. *J. Neurosci.* **37**, 11835–11853 (2017).

1060 69. C. Kim, S. Kwon, M. Iba, B. Spencer, E. Rockenstein, M. Mante, A. Adame, S. J. Shin, J.
1061 A. Fields, R. A. Rissman, S.-J. Lee, E. Masliah, Effects of innate immune receptor
1062 stimulation on extracellular α-synuclein uptake and degradation by brain resident cells.
1063 *Exp. Mol. Med.* **53**, 281–290 (2021).

1064 70. D. Gussakovsky, S. A. McKenna, Alu RNA and their roles in human disease states. *RNA*
1065 *Biol.* **18**, 574–585 (2021).

1066 71. R. La Piana, C. Uggetti, I. Olivieri, D. Tonduti, U. Balottin, E. Fazzi, S. Orcesi, Bilateral
1067 striatal necrosis in two subjects with Aicardi-Goutières syndrome due to mutations in
1068 ADAR1 (AGS6). *Am. J. Med. Genet. A.* **164A**, 815–819 (2014).

1069 72. Q. Li, M. J. Gloudemans, J. M. Geisinger, B. Fan, F. Aguet, T. Sun, G. Ramaswami, Y. I. Li,
1070 J.-B. Ma, J. K. Pritchard, S. B. Montgomery, J. B. Li, RNA editing underlies genetic risk of
1071 common inflammatory diseases. *Nature* **608**, 569–577 (2022).

1072 73. K. S. Levine, H. L. Leonard, C. Blauwendraat, H. Iwaki, N. Johnson, S. Bandres-Ciga, L.
1073 Ferrucci, F. Faghri, A. B. Singleton, M. A. Nalls, Virus exposure and neurodegenerative
1074 disease risk across national biobanks. *Neuron* **111**, 1086-1093.e2 (2023).

1075 74. W. Hoyer, T. Antony, D. Cherny, G. Heim, T. M. Jovin, V. Subramaniam, Dependence of
1076 α-Synuclein Aggregate Morphology on Solution Conditions. *J. Mol. Biol.* **322**, 383–393
1077 (2002).

1078 75. M. J. Devine, M. Ryten, P. Vodicka, A. J. Thomson, T. Burdon, H. Houlden, F. Cavaleri,
1079 M. Nagano, N. J. Drummond, J.-W. Taanman, A. H. Schapira, K. Gwinn, J. Hardy, P. A.
1080 Lewis, T. Kunath, Parkinson's disease induced pluripotent stem cells with triplication of
1081 the α-synuclein locus. *Nat. Commun.* **2**, 440 (2011).

1082 76. K. Gupta, R. Patani, P. Baxter, A. Serio, D. Story, T. Tsujita, J. D. Hayes, R. A. Pedersen,
1083 G. E. Hardingham, S. Chandran, Human embryonic stem cell derived astrocytes mediate
1084 non-cell-autonomous neuroprotection through endogenous and drug-induced
1085 mechanisms. *Cell Death Differ.* **19**, 779–787 (2012).

1086 77. N. Seto-Salvia, N. Esteras, R. de Silva, E. de Pablo-Fernandez, C. Arber, C. E. Toomey, J.
1087 M. Polke, H. R. Morris, J. D. Rohrer, R. Patani, S. Wray, T. T. Warner, Elevated 4R-tau in
1088 Astrocytes From Asymptomatic Carriers of the MAPT 10+16 Mutation. *Res. Sq.*, doi:
1089 10.21203/rs.3.rs-117443/v1 (2020).

1090 78. Y. Shi, P. Kirwan, J. Smith, H. P. C. Robinson, F. J. Livesey, Human cerebral cortex
1091 development from pluripotent stem cells to functional excitatory synapses. *Nat.*
1092 *Neurosci.* **15**, 477–486 (2012).

1093 79. O. Kopach, N. Esteras, S. Wray, A. Y. Abramov, D. A. Rusakov, Genetically engineered
1094 MAPT 10+16 mutation causes pathophysiological excitability of human iPSC-derived
1095 neurons related to 4R tau-induced dementia. *Cell Death Dis.* **12**, 1–12 (2021).

1096 80. O. Kopach, N. Esteras, S. Wray, D. A. Rusakov, A. Y. Abramov, Maturation and
1097 phenotype of pathophysiological neuronal excitability of human cells in tau-related
1098 dementia. *J. Cell Sci.* **133**, jcs241687 (2020).

1099 81. O. Kopach, Y. Dobropolska, P. Belan, N. Voitenko, Ca2+-Permeable AMPA Receptors
1100 Contribute to Changed Dorsal Horn Neuronal Firing and Inflammatory Pain. *Int. J. Mol.*
1101 *Sci.* **24**, 2341 (2023).

1102 82. A. Butler, P. Hoffman, P. Smibert, E. Papalexi, R. Satija, Integrating single-cell
1103 transcriptomic data across different conditions, technologies, and species. *Nat.*
1104 *Biotechnol.* **36**, 411–420 (2018).

1105 83. T. Stuart, A. Butler, P. Hoffman, C. Hafemeister, E. Papalexi, W. M. Mauck, Y. Hao, M.
1106 Stoeckius, P. Smibert, R. Satija, Comprehensive Integration of Single-Cell Data. *Cell* **177**,
1107 1888-1902.e21 (2019).

1108 84. L. Zappia, A. Oshlack, Clustering trees: a visualization for evaluating clusterings at
1109 multiple resolutions. *GigaScience* **7**, giy083 (2018).

1110 85. S. Chen, Y. Zhou, Y. Chen, J. Gu, fastp: an ultra-fast all-in-one FASTQ preprocessor.
1111 *Bioinformatics* **34**, i884–i890 (2018).

1112 86. A. Dobin, C. A. Davis, F. Schlesinger, J. Drenkow, C. Zaleski, S. Jha, P. Batut, M. Chaisson,
1113 T. R. Gingeras, STAR: ultrafast universal RNA-seq aligner. *Bioinformatics* **29**, 15–21
1114 (2013).

1115 87. A. D. Yates, P. Achuthan, W. Akanni, J. Allen, J. Allen, J. Alvarez-Jarreta, M. R. Amode, I.
1116 M. Armean, A. G. Azov, R. Bennett, J. Bhai, K. Billis, S. Boddu, J. C. Marugán, C. Cummins,
1117 C. Davidson, K. Dodiya, R. Fatima, A. Gall, C. G. Giron, L. Gil, T. Grego, L. Haggerty, E.
1118 Haskell, T. Hourlier, O. G. Izuogu, S. H. Janacek, T. Juettemann, M. Kay, I. Lavidas, T. Le,
1119 D. Lemos, J. G. Martinez, T. Maurel, M. McDowall, A. McMahon, S. Mohanan, B. Moore,

1120 M. Nuhn, D. N. Oheh, A. Parker, A. Parton, M. Patricio, M. P. Sakthivel, A. I. Abdul Salam,
1121 B. M. Schmitt, H. Schuilenburg, D. Sheppard, M. Sycheva, M. Szuba, K. Taylor, A.
1122 Thormann, G. Threadgold, A. Vullo, B. Walts, A. Winterbottom, A. Zadissa, M.
1123 Chakiachvili, B. Flint, A. Frankish, S. E. Hunt, G. IIsley, M. Kostadima, N. Langridge, J. E.
1124 Loveland, F. J. Martin, J. Morales, J. M. Mudge, M. Muffato, E. Perry, M. Ruffier, S. J.
1125 Trevanion, F. Cunningham, K. L. Howe, D. R. Zerbino, P. Flicek, Ensembl 2020. *Nucleic*
1126 *Acids Res.* **48**, D682–D688 (2020).

1127 88. L. Wang, S. Wang, W. Li, RSeQC: quality control of RNA-seq experiments. *Bioinformatics*
1128 **28**, 2184–2185 (2012).

1129 89. P. Ewels, M. Magnusson, S. Lundin, M. Käller, MultiQC: summarize analysis results for
1130 multiple tools and samples in a single report. *Bioinformatics* **32**, 3047–3048 (2016).

1131 90. R. Patro, G. Duggal, M. I. Love, R. A. Irizarry, C. Kingsford, Salmon provides fast and bias-
1132 aware quantification of transcript expression. *Nat. Methods* **14**, 417–419 (2017).

1133 91. C. Soneson, M. I. Love, M. D. Robinson, Differential analyses for RNA-seq: transcript-
1134 level estimates improve gene-level inferences. F1000Research 4:1521 [Preprint]
1135 (2016). https://doi.org/10.12688/f1000research.7563.2.

1136 92. M. I. Love, W. Huber, S. Anders, Moderated estimation of fold change and dispersion
1137 for RNA-seq data with DESeq2. *Genome Biol.* **15**, 550 (2014).

1138 93. Y. I. Li, D. A. Knowles, J. Humphrey, A. N. Barbeira, S. P. Dickinson, H. K. Im, J. K.
1139 Pritchard, Annotation-free quantification of RNA splicing using LeafCutter. *Nat. Genet.*
1140 **50**, 151–158 (2018).

1141 94. H. M. Amemiya, A. Kundaje, A. P. Boyle, The ENCODE Blacklist: Identification of
1142 Problematic Regions of the Genome. *Sci. Rep.* **9**, 9354 (2019).

1143 95. D. Zhang, R. H. Reynolds, S. Garcia-Ruiz, E. K. Gustavsson, S. Sethi, S. Aguti, I. A. Barbosa,
1144 J. J. Collier, H. Houlden, R. McFarland, F. Muntoni, M. Oláhová, J. Poulton, M. Simpson,
1145 R. D. S. Pitceathly, R. W. Taylor, H. Zhou, C. Deshpande, J. A. Botia, L. Collado-Torres,
1146 M. Ryten, Detection of pathogenic splicing events from RNA-sequencing data using
1147 dasper. bioRxiv [Preprint] (2021). https://doi.org/10.1101/2021.03.29.437534.

1148 96. clusterProfiler: an R Package for Comparing Biological Themes Among Gene Clusters |
1149 OMICS: A Journal of Integrative Biology.
1150 https://www.liebertpub.com/doi/full/10.1089/omi.2011.0118.

1151 97. The UniProt Consortium, UniProt: the Universal Protein Knowledgebase in 2023.
1152 *Nucleic Acids Res.* **51**, D523–D531 (2023).

1153 98. E. K. Gustavsson, D. Zhang, R. H. Reynolds, S. Garcia-Ruiz, M. Ryten, ggtranscript: an R
1154 package for the visualization and interpretation of transcript isoforms using ggplot2.
1155 *Bioinformatics* **38**, 3844–3846 (2022).

1156 99. M. Piechotta, E. Wyler, U. Ohler, M. Landthaler, C. Dieterich, JACUSA: site-specific
1157 identification of RNA editing events from replicate sequencing data. *BMC*
1158 *Bioinformatics* **18**, 7 (2017).

1159 100. M. Piechotta, I. S. Naarmann-de Vries, Q. Wang, J. Altmüller, C. Dieterich, RNA
1160 modification mapping with JACUSA2. *Genome Biol.* **23**, 115 (2022).

1161 101. O. Tange, GNU Parallel 20230722 ('Пригóжин'), Zenodo (2023);
1162 https://doi.org/10.5281/zenodo.8175685.

1163 102. P. Danecek, J. K. Bonfield, J. Liddle, J. Marshall, V. Ohan, M. O. Pollard, A. Whitwham,
1164 T. Keane, S. A. McCarthy, R. M. Davies, H. Li, Twelve years of SAMtools and BCFtools.
1165 *GigaScience* **10**, giab008 (2021).

1166 103. W. McLaren, L. Gil, S. E. Hunt, H. S. Riat, G. R. S. Ritchie, A. Thormann, P. Flicek, F.
1167 Cunningham, The Ensembl Variant Effect Predictor. *Genome Biol.* **17**, 122 (2016).

1168 104. D. Nishimura, RepeatMasker. *Biotech Softw. Internet Rep.* **1**, 36–39 (2000).

1169 105. R. Feleke, R. H. Reynolds, A. M. Smith, B. Tilley, S. A. G. Taliun, J. Hardy, P. M. Matthews,
1170 S. Gentleman, D. R. Owen, M. R. Johnson, P. K. Srivastava, M. Ryten, Cross-platform
1171 transcriptional profiling identifies common and distinct molecular pathologies in Lewy
1172 body diseases. *Acta Neuropathol. (Berl.)* **142**, 449–474 (2021).

1173 106. F. A. Wolf, P. Angerer, F. J. Theis, SCANPY: large-scale single-cell gene expression data
1174 analysis. *Genome Biol.* **19**, 15 (2018).

1175

1176

1177 Acknowledgements

1178 We would like to thank the donors for their fibroblast and brain tissue donation. We would
1179 also like to thank the Francis Crick Institute Flow Cytometry, Advanced Light Microscopy,
1180 Advanced Sequencing, and Bioinformatics and Biostatistics STPs for their help and equipment
1181 in conducting and analysing the flow cytometry, fluorescence microscopy, and single-cell
1182 RNA-seq experiments. This research was funded in whole or in part by Aligning Science Across
1183 Parkinson's [ASAP-000509 and ASAP-000463] through the Michael J. Fox Foundation for
1184 Parkinson's Research (MJFF). AZW was supported through the award of a Clinical Research
1185 Fellowship funded by the Wolfson Foundation and Eisai Ltd. SG was supported by Wellcome
1186 (100172/Z/12/2) and is currently an MRC Senior Clinical Fellow (MR/T008199/1). MR was
1187 supported by the UK Medical Research Council (MRC) through her award of Tenure-track

Clinician Scientist Fellowship (MR/N008324/1). This work was funded in part by a grant from MJFF (Project Title: Reacting to alpha-synuclein: how astrocytes cause neuronal loss in Parkinson's Disease; Grant ID: 18004).

Competing interests

Author RHR is currently employed by CoSyne Therapeutics (Lead Bioinformatician). All work performed for this publication was performed in her own time, and not as a part of her duties as an employee.

Data availability

The data that support the findings of this study are available at https://zenodo.org/records/10608268. Bulk-tissue and single-cell RNA-sequencing data will be accessible through the European Genome–phenome Archive. The RNA editing results are available at https://zenodo.org/records/10630845. Protocols used in this study can be found in the repository Protocols.io and the DOIs can be found in Supplementary Table 14.

Code availability

Code used for the analyses of bulk-tissue and single cell RNA-sequencing data is available at https://github.com/karishdsa/ipscAstrNeurCocul. Code for the RNA editing analyses is available at https://github.com/aaronwagen/Astrocytes_editing.

Ethics declaration

iPSCs lines were obtained from a number of different sources, commercially, from repositories (part of the EU IMI-funded program StemBANCC), or generated from fibroblasts from in-house skin biopsies taken under informed consent.

Figures

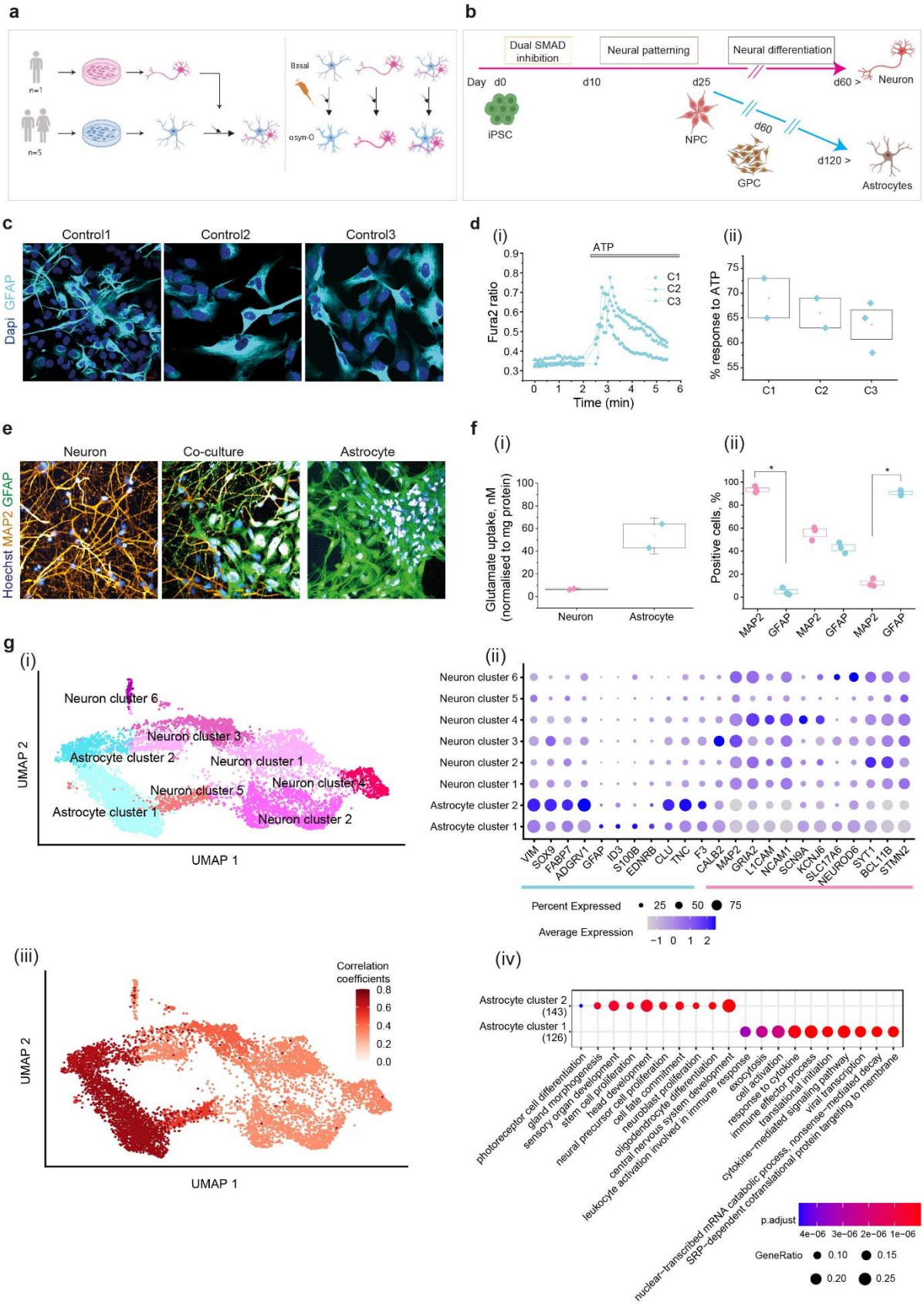
a
n=1
n=5
Basal
α-syn-O
b
Dual SMAD inhibition
Neural patterning
Neural differentiation
Day d0
d10
d25
d60 >
Neuron
iPSC
NPC
d60
GPC
d120 >
Astrocytes
c
Control1
Control2
Control3
Dapi GFAP
d
(i)
ATP
Fura2 ratio
C1
C2
C3
Time (min)
(ii)
% response to ATP
e
Neuron
Co-culture
Astrocyte
Hoechst MAP2 GFAP
f
(i)
Glutamate uptake, nM (normalised to mg protein)
Neuron
Astrocyte
(ii)
Positive cells, %
MAP2
GFAP
g
(i)
UMAP 2
UMAP 1
Neuron cluster 6
Neuron cluster 3
Astrocyte cluster 2
Neuron cluster 1
Neuron cluster 4
Neuron cluster 5
Astrocyte cluster 1
Neuron cluster 2
(ii)
Neuron cluster 6
Neuron cluster 5
Neuron cluster 4
Neuron cluster 3
Neuron cluster 2
Neuron cluster 1
Astrocyte cluster 2
Astrocyte cluster 1
VIM
SOX9
FABP7
ADGRV1
GFAP
ID3
S100B
EDNRB
CLU
TNC
F3
CALB2
MAP2
GRIA2
L1CAM
NCAM1
SCN9A
KCNJ6
SLC17A6
NEUROD6
SYT1
BCL11B
STMN2
Percent Expressed
25
50
75
Average Expression
−1
0
1
2
(iii)
Correlation coefficients
0.8
0.6
0.4
0.2
0.0
UMAP 2
UMAP 1
(iv)
Astrocyte cluster 2 (143)
Astrocyte cluster 1 (126)
photoreceptor cell differentiation
gland morphogenesis
sensory organ development
stem cell proliferation
head development
cell proliferation
neural precursor cell proliferation
cell fate commitment
neuroblast proliferation
oligodendrocyte differentiation
central nervous system development
leukocyte activation involved in immune response
exocytosis
cell activation
response to cytokine
immune effector process
translational initiation
cytokine−mediated signaling pathway
viral transcription
nuclear−transcribed mRNA catabolic process, nonsense−mediated decay
SRP−dependent cotranslational protein targeting to membrane
p.adjust
4e−06
3e−06
2e−06
1e−06
GeneRatio
0.10
0.15
0.20
0.25

1218

1219 **Fig 1. Schematic illustrations of experimental paradigm and the differentiation protocols.**
1220 (a) hiPSC-derived from five healthy individuals are differentiated into astrocytes (in-house
1221 lines: C1, C2, C3, commercial lines from ACS: C4, C5) and from one individual into neurons. (b)
1222 Differentiation of cortical region-specific astrocytes was performed, modifying established
1223 protocols.(*76*, *77*) Neural precursor cells (NPCs) using an established protocol (Shi et al., 2012)
1224 were differentiated into either neurons and GPC (glial precursor cells) after 30 days from NPC,
1225 then further differentiated into mature astrocytes. (c) Immunocytochemistry images show
1226 that three lines of hiPSC-derived astrocytes express the astrocytic marker, GFAP. (di-ii) There
1227 is a calcium response to APT in iPSC-derived astrocytes. Representative traces of calcium (di)
1228 and the percentage of cells (dii) in response to ATP. (e) hiPSC-derived astrocyte enables
1229 uptake of glutamate (Glutamate Assay Kit, (ab83389/K629-100, Abcam). (fi-ii) Composition of
1230 hiPSC-derived neuron and astrocyte co-culture assessed using MAP2 (neuronal marker) and
1231 GFAP (astrocytic marker) immunocytochemistry together with representative images of a
1232 neuronal, astrocyte and co-culture (fi) and the quantification (fii). (g) (i)UMAP plot showing
1233 the clustering of the integrated dataset using the cells from all the samples (basal and αsyn-
1234 O treated astrocytes, neurons, co-culture samples). (ii) Dot plots showing the expression of
1235 the astrocyte and neuron marker genes in the clusters identified in the single-cell RNA-Seq
1236 data. (iii) UMAP overlaid with the correlation coefficients, showing the correlation of the 2
1237 astrocyte clusters with the astrocytes from Leng et al.(*27*) (iv) GO terms associated with the
1238 genes up-regulated in Astrocyte clusters 1 and 2.
1239
1240
1241

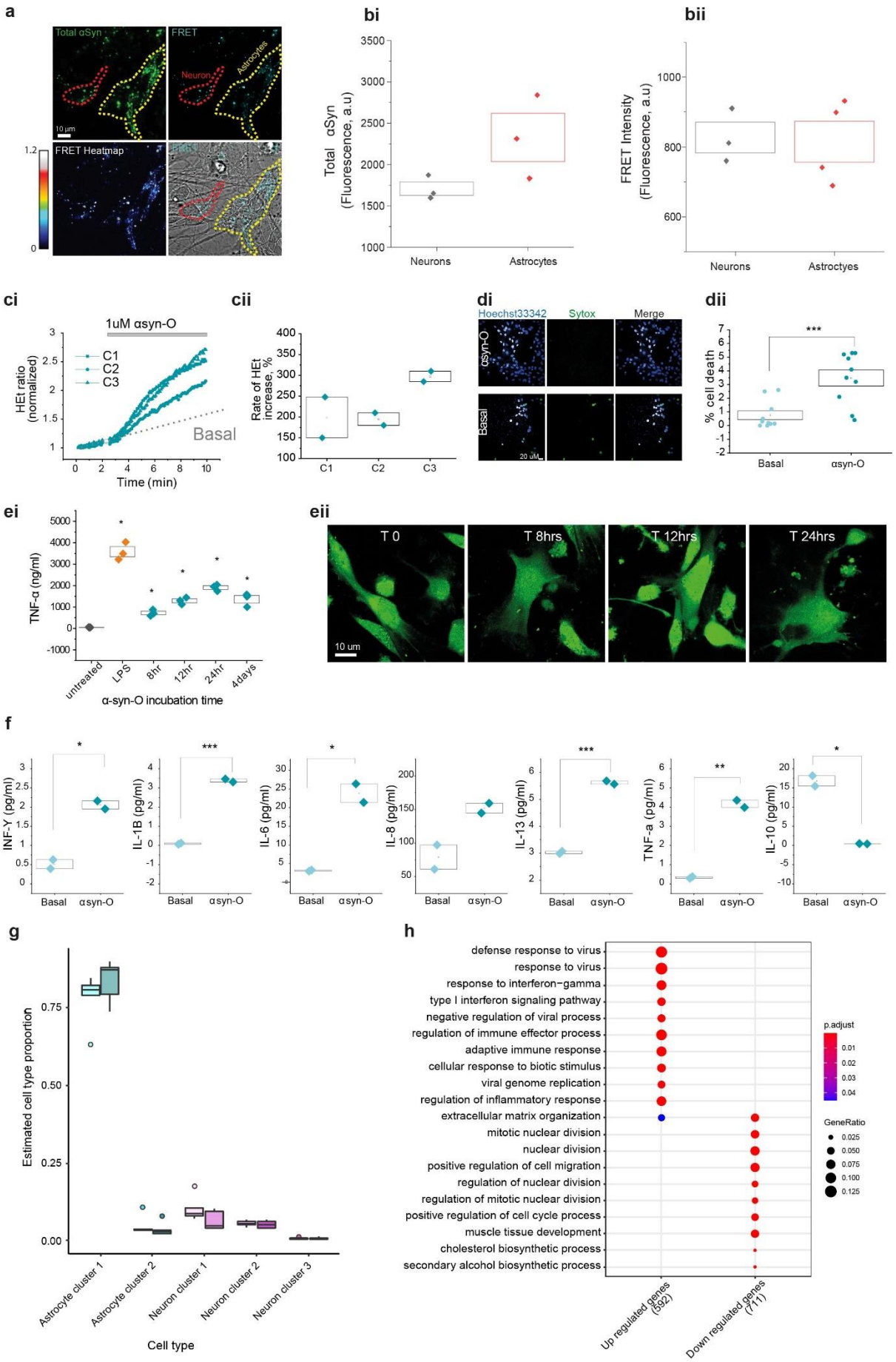
a
Total αSyn
FRET
Neuron
Astrocytes
10 µm
FRET Heatmap
1.2
0
bi
Total αSyn (Fluorescence, a.u)
Neurons
Astrocytes
bii
FRET Intensity (Fluorescence, a.u)
Neurons
Astroctyes
ci
1uM αsyn-O
HEt ratio (normalized)
C1
C2
C3
Basal
Time (min)
cii
Rate of HEt increase, %
C1
C2
C3
di
Hoechst33342
Sytox
Merge
αsyn-O
Basal
20 uM
dii
% cell death
***
Basal
αsyn-O
ei
TNF-α (ng/ml)
untreated
LPS
8hr
12hr
24hr
4days
α-syn-O incubation time
eii
T 0
T 8hrs
T 12hrs
T 24hrs
10 um
f
INF-Y (pg/ml)
IL-1B (pg/ml)
IL-6 (pg/ml)
IL-8 (pg/ml)
IL-13 (pg/ml)
TNF-a (pg/ml)
IL-10 (pg/ml)
Basal
αsyn-O
g
Estimated cell type proportion
Astrocyte cluster 1
Astrocyte cluster 2
Neuron cluster 1
Neuron cluster 2
Neuron cluster 3
Cell type
h
defense response to virus
response to virus
response to interferon−gamma
type I interferon signaling pathway
negative regulation of viral process
regulation of immune effector process
adaptive immune response
cellular response to biotic stimulus
viral genome replication
regulation of inflammatory response
extracellular matrix organization
mitotic nuclear division
nuclear division
positive regulation of cell migration
regulation of nuclear division
regulation of mitotic nuclear division
positive regulation of cell cycle process
muscle tissue development
cholesterol biosynthetic process
secondary alcohol biosynthetic process
Up regulated genes (592)
Down regulated genes (711)
p.adjust
GeneRatio

1243 **Fig 2 Oligomer treatment of astrocytes induces an inflammatory state.**
1244 (a) Uptake of monomeric species of labelled α-syn (A53T monomer) in astrocytes (with yellow
1245 dotted lines) and neurons (with red dotted lines) was detected, and the formation of
1246 oligomers inside cells confirmed using the FRET biosensor. (bi-ii) There is no difference in the
1247 formation of oligomeric species despite the higher uptake of total α-syn in astrocytes
1248 compared to neurons (n = 3 independent inductions). (ci-ii) Application of αsyn-O induces the
1249 overproduction of reactive oxygen species (ROS). (di-ii) Cell death induced by αsyn-O is
1250 detected in astrocytes at low levels. (ei) αsyn-O treated astrocytes release cytokine
1251 responding to αsyn-O (measured by variable incubation time and the representative images).
1252 Cytokine release is time-dependent, with the level of TNF- α highest after 24hr incubation
1253 with αsyn-O. (eii) Morphological changes were traced using Fluo4 across the same time
1254 course as the cytokine release measurements. (fi-vii) αsyn-O treated astrocytes induce an
1255 inflammatory state by releasing a range of cytokines responding to αsyn-O (basal IL-13: 3.02
1256 ± 0.04 pg/ml, αsyn-O treated 5.62 ± 0.05 pg/ml, IL-6: basal 3.11 ± 0.13 pg/ml, αsyn-O treated
1257 23.8 ± 2.4 pg/ml, IL-8: basal 79.11 ±18.07 pg/ml, αsyn-O treated: 152.01 ± 7.29 pg/ml, IL-1B:
1258 basal 0.955 ± 0.03011, αsyn-O treated 3.38 ± 0.0772, INF-Y: basal 0.51 ± 0.11, αsyn-O treated
1259 2.05 ± 0.1 pg/ml, TNF-α: basal 0.33 ± 0.0414, αsyn-O treated 4.16 ± 0.187) (g) Cell type
1260 proportions derived from deconvolution using Scaden. The plot shows the cell type
1261 proportion for each of the cell types in the bulk astrocyte samples, basally and with αsyn-O
1262 treatment, as predicted by Scaden. Cell types with proportions < 1% were excluded. (h) The
1263 top 10 GO terms associated with up and down-regulated differentially expressed genes at
1264 FDR < 5% and with at least >= 2-fold change in expression in the astrocytes basally vs with
1265 αsyn-O treatment.

1266

1267

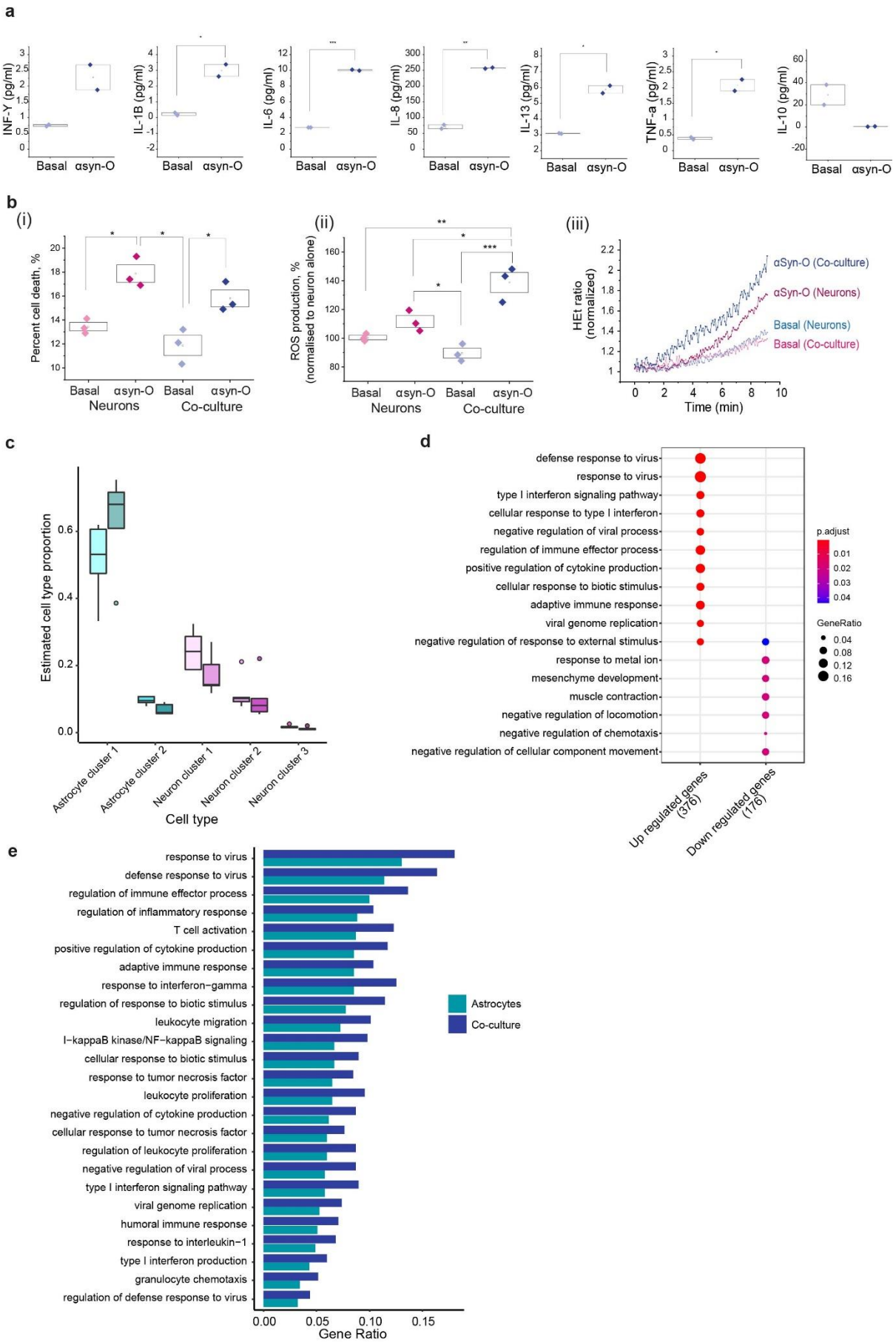
a
INF-Y (pg/ml)
IL-1B (pg/ml)
IL-6 (pg/ml)
IL-8 (pg/ml)
IL-13 (pg/ml)
TNF-a (pg/ml)
IL-10 (pg/ml)
Basal
αsyn-O
b
(i)
Percent cell death, %
Basal
αsyn-O
Neurons
Co-culture
(ii)
ROS production, %
(normalised to neuron alone)
(iii)
HEt ratio
(normalized)
αSyn-O (Co-culture)
αSyn-O (Neurons)
Basal (Neurons)
Basal (Co-culture)
Time (min)
c
Estimated cell type proportion
Astrocyte cluster 1
Astrocyte cluster 2
Neuron cluster 1
Neuron cluster 2
Neuron cluster 3
Cell type
d
defense response to virus
response to virus
type I interferon signaling pathway
cellular response to type I interferon
negative regulation of viral process
regulation of immune effector process
positive regulation of cytokine production
cellular response to biotic stimulus
adaptive immune response
viral genome replication
negative regulation of response to external stimulus
response to metal ion
mesenchyme development
muscle contraction
negative regulation of locomotion
negative regulation of chemotaxis
negative regulation of cellular component movement
Up regulated genes (376)
Down regulated genes (176)
p.adjust
GeneRatio
e
response to virus
defense response to virus
regulation of immune effector process
regulation of inflammatory response
T cell activation
positive regulation of cytokine production
adaptive immune response
response to interferon−gamma
regulation of response to biotic stimulus
leukocyte migration
I−kappaB kinase/NF−kappaB signaling
cellular response to biotic stimulus
response to tumor necrosis factor
leukocyte proliferation
negative regulation of cytokine production
cellular response to tumor necrosis factor
regulation of leukocyte proliferation
negative regulation of viral process
type I interferon signaling pathway
viral genome replication
humoral immune response
response to interleukin−1
type I interferon production
granulocyte chemotaxis
regulation of defense response to virus
Astrocytes
Co-culture
Gene Ratio

1268

1269

1270 **Fig 3 Co-culture setting provides evidence of the astrocytes becoming more inflammatory.**
1271 (a) Effect of αsyn-O on cytokine release in the co-cultures (basal IL-13: 3.091 ± 0.0139 pg/ml,
1272 αsyn-O treated 5.88 ± 0.238 pg/ml, IL-6: basal 2.75 ± 0.00174 pg/ml, αsyn-O treated 10.026
1273 ± 0.0593 pg/ml, IL-8: basal 71.09 ± 6.107 pg/ml, αsyn-O treated 257.2 ± 1.58 pg/ml, IL-1B:
1274 basal: 0.231 ± 0.0835 pg/ml, αsyn-O treated 2.99 ± 0.381 pg/ml, INF-Y: basal 0.392 ± 0.0329,
1275 αsyn-O treated 2.078 ± 0.180 pg/ml, TNF-α: basal 0.392 ± 0.0329, αsyn-O treated 2.078 ±
1276 0.1801) (bi-iii) αsyn-O induces toxicity in neurons alone and in co-culture with astrocytes, and
1277 induces increased levels of ROS in neurons alone and in co-culture . (c) Plot showing the cell
1278 type proportions estimated by Scaden from the single cell data in the co-culture samples,
1279 basally (lighter shade) and with αsyn-O treatment (darker shade). There is a significant
1280 difference between the cell type proportions of astrocyte cluster 1 and 2 in the co-culture
1281 with αsyn-O treated compared to basal. (d) GO terms associated with the up- and down-
1282 regulated differentially expressed genes with at least >= 2-fold change in expression in the co-
1283 culture αsyn-O treated vs basal (e) Visualising gene ratios of the enrichments observed in the
1284 up-regulated differentially expressed genes of the astrocytes (cyan) compared to that of the
1285 co-culture (blue).

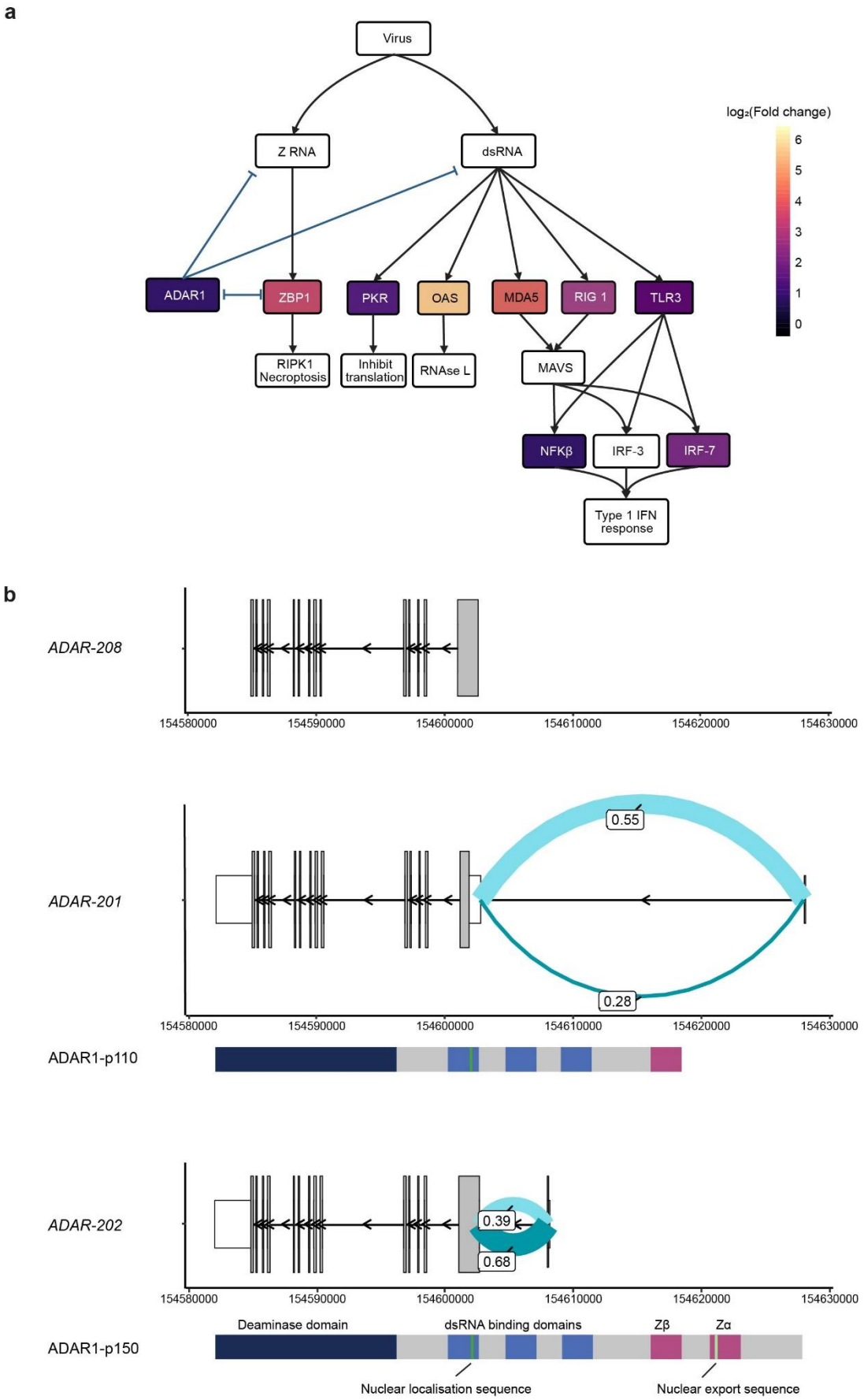
a
Virus
Z RNA
dsRNA
log₂(Fold change)
6
5
4
3
2
1
0
ADAR1
ZBP1
PKR
OAS
MDA5
RIG 1
TLR3
RIPK1 Necroptosis
Inhibit translation
RNAse L
MAVS
NFKβ
IRF-3
IRF-7
Type 1 IFN response
b
ADAR-208
154580000
154590000
154600000
154610000
154620000
154630000
ADAR-201
0.55
0.28
ADAR1-p110
ADAR-202
0.39
0.68
ADAR1-p150
Deaminase domain
dsRNA binding domains
Zβ
Zα
Nuclear localisation sequence
Nuclear export sequence

1286

1287 **Fig 4 Type 1 IFN response leads to activation of *ADAR*** (a) Model summarizing the role of
1288 *ADAR* in regulating the innate immune response to dsRNA with the $\log_2$(Fold change) of the
1289 genes that are significantly differentially expressed (at FDR < 5%) in the astrocytes on αsyn-
1290 O treatment. (b) Plot showing the significantly differentially spliced junctions in *ADAR* in the
1291 astrocytes on αsyn-O treatment, with the transcripts and protein isoforms. (Co-culture: **Supp**
1292 **figure 5a, b**).
1293

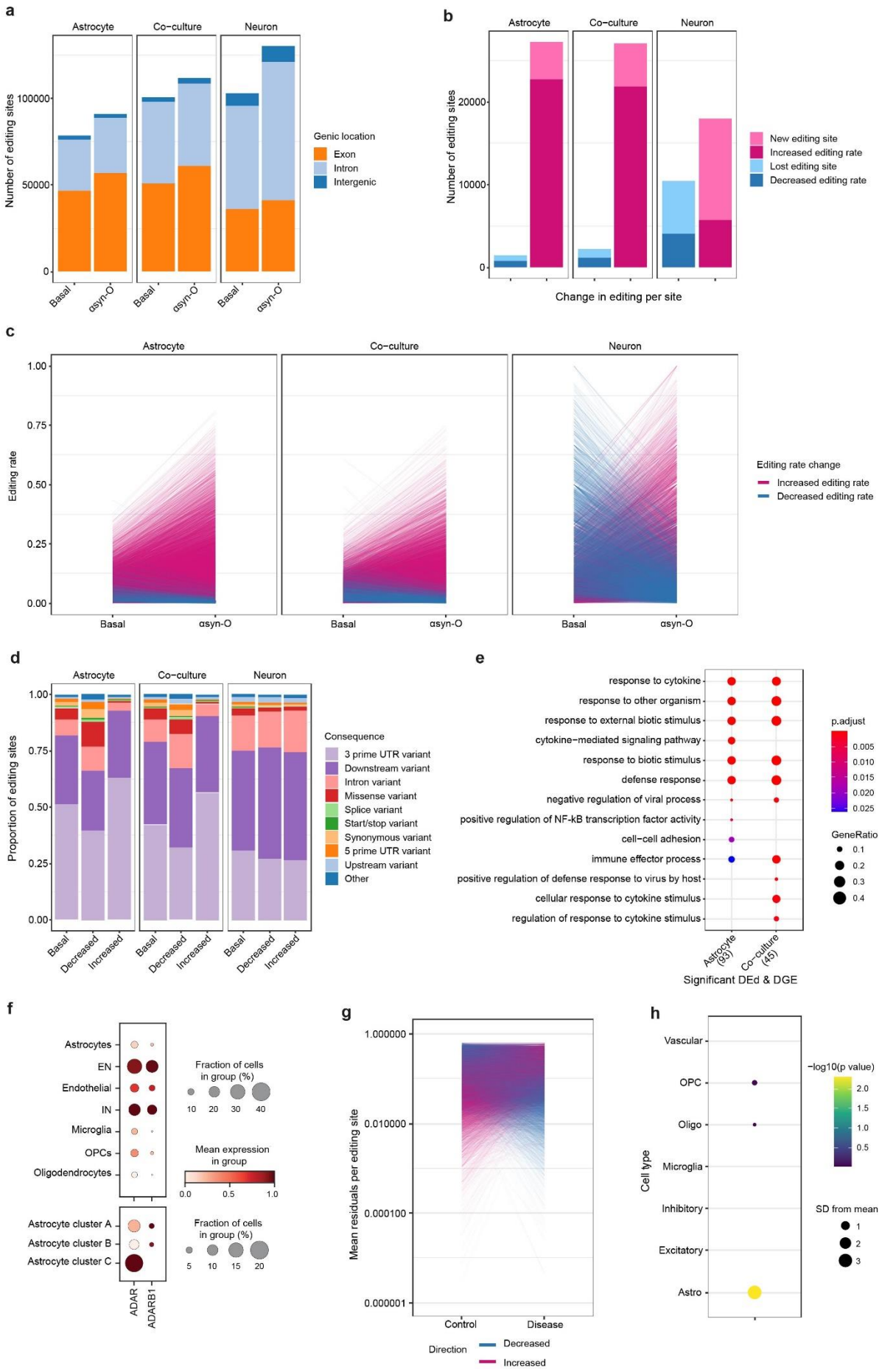
a
Astrocyte
Co−culture
Neuron
Number of editing sites
100000
50000
0
Basal
αsyn-O
Genic location
Exon
Intron
Intergenic
b
Astrocyte
Co−culture
Neuron
Number of editing sites
20000
10000
0
Change in editing per site
New editing site
Increased editing rate
Lost editing site
Decreased editing rate
c
Astrocyte
Co−culture
Neuron
Editing rate
1.00
0.75
0.50
0.25
0.00
Basal
αsyn-O
Editing rate change
Increased editing rate
Decreased editing rate
d
Astrocyte
Co−culture
Neuron
Proportion of editing sites
1.00
0.75
0.50
0.25
0.00
Basal
Decreased
Increased
Consequence
3 prime UTR variant
Downstream variant
Intron variant
Missense variant
Splice variant
Start/stop variant
Synonymous variant
5 prime UTR variant
Upstream variant
Other
e
response to cytokine
response to other organism
response to external biotic stimulus
cytokine−mediated signaling pathway
response to biotic stimulus
defense response
negative regulation of viral process
positive regulation of NF-kB transcription factor activity
cell−cell adhesion
immune effector process
positive regulation of defense response to virus by host
cellular response to cytokine stimulus
regulation of response to cytokine stimulus
Astrocyte (93)
Co−culture (45)
Significant DEd & DGE
p.adjust
0.005
0.010
0.015
0.020
0.025
GeneRatio
0.1
0.2
0.3
0.4
f
Astrocytes
EN
Endothelial
IN
Microglia
OPCs
Oligodendrocytes
Fraction of cells in group (%)
10
20
30
40
Mean expression in group
0.0
0.5
1.0
Astrocyte cluster A
Astrocyte cluster B
Astrocyte cluster C
Fraction of cells in group (%)
5
10
15
20
ADAR
ADARB1
g
Mean residuals per editing site
1.000000
0.010000
0.000100
0.000001
Control
Disease
Direction
Decreased
Increased
h
Vascular
OPC
Oligo
Microglia
Inhibitory
Excitatory
Astro
Cell type
−log10(p value)
2.0
1.5
1.0
0.5
SD from mean
1
2
3

1294

Fig 5 *ADAR* induced in A to I editing in astrocytes and co-cultures with αsyn-O treatment. (a) Number of editing sites in each sample, showing genomic locations (b) Number of differentially edited sites when comparing αsyn-O treated to samples basally in each culture. X-axis shows the decreased editing (blue, including lost) and increased editing (pink, including new). (c) Change in editing rate in basal vs αsyn-O treated samples in each culture. (d) Consequences of editing sites at baseline, and in differentially decreased or increased sites across cultures. (e) GO terms associated with the significantly differentially edited and differentially expressed (FDR < 5% and FC >=2) in the astrocytes and co-culture αsyn-O, treated vs basal. (f) Expression of *ADAR* and *ADARB1* in single nuclear post-mortem brain RNA. The top panel shows expression by cell-type, and the bottom shows expression within astrocytic clusters. Astrocyte cluster A is defined by expression of *ADGRV1* and *SLC1A2*; Astrocyte cluster B by *GFAP*, *S100B*, *AQP4* and Astrocyte cluster C by *VIM*, *SOX9* and *FOS*. (g) Mean residuals per editing site, after correction for covariates, in controls and diseased PD post-mortem brain samples. (h) Expression weighted celltype enrichment analysis of genes with 50 greatest increase in mean editing rate.

Abbreviations: EN - excitatory neurons. IN - inhibitory neurons. OPC - oligodendrocyte progenitor cells.

Supplementary Figures- Supp fig1 to Supp fig 7

Supplementary figures

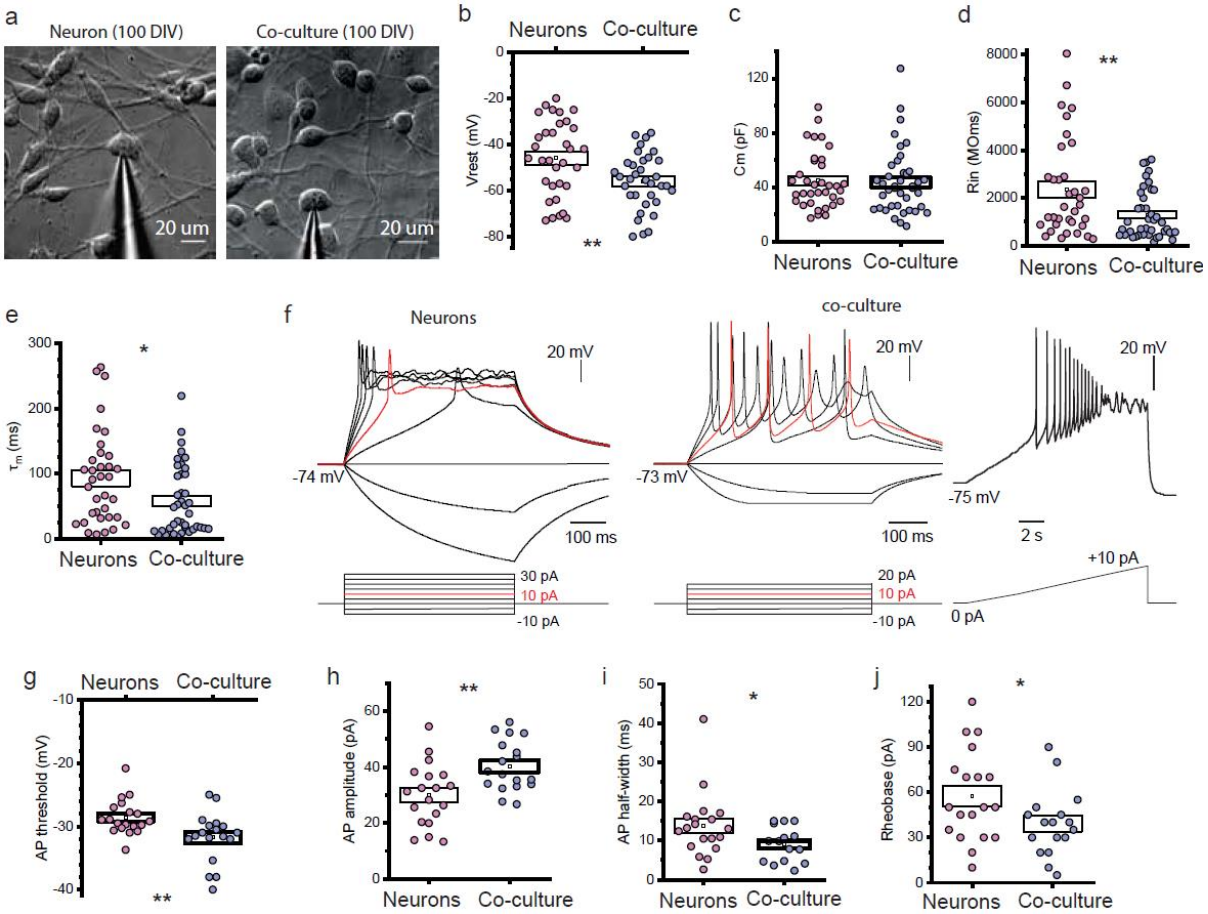

Supp Fig 1

(a) Transmitted light images of iPSC-derived cells in neuronal culture (left) and neuron-astrocytic co-culture (right) for whole-cell recordings made from individual neurons using patch pipettes. (b) Statistical summary of the resting membrane potential (Vrest) revealed more hyperpolarised Vrest of iPSC-derived cortical neurons in co-cultures than in the corresponding age-matched cultures. (c - e) Passive membrane properties of iPSC-derived cortical neurons showed similar cell capacity (Cm, Fig 3.c), but different membrane constant (τm, Fig 3.e) and input resistance (Rin, Fig 3.d) between neuronal cultures and co-cultures, indicating a difference in biophysical maturation of the neurons. All data are mean with s.e.m. *P < 0.05, **p < 0.01 (the two-tailed unpaired t-test). (f) Representative recordings of action potential (AP) firing in an iPSC-derived neuron evoked by a series of rectangular depolarising current pulses of increased intensity (indicated on the bottom) in cultures. (Bii) Example recordings of AP discharge generated by an iPSC-derived neuron evoked by square depolarising current pulses (left traces) or a slow-ramp current (indicated on the bottom) in co-cultures. Note a train of evoked APs in co-cultures.

Analysis of individual APs across iPSC-derived cortical neurons revealed significant changes in the threshold (g), spike amplitude (h), half-width kinetic parameters (i), and rheobase (j).

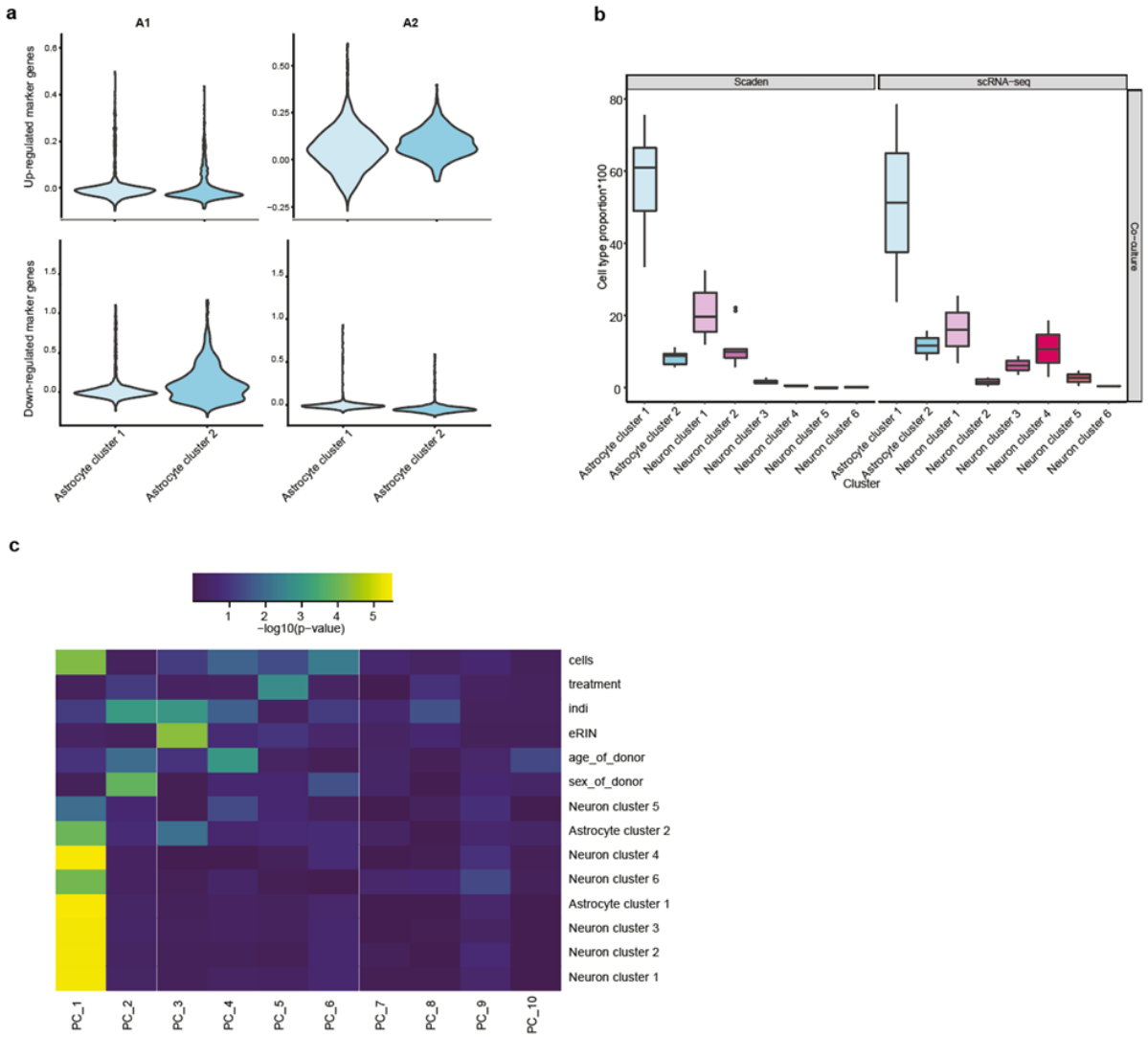

Supp Fig 2

(a) Visualising the module score of the published up and down regulated A1 and A2 marker genes in astrocyte clusters 1 and 2. The module score, generated per cell for a set of genes using the AddModuleScore() in Seurat, is the difference between the average expression of each gene set and random control genes, per cell. (b) Cell type proportions estimated by the single cell data vs that predicted by Scaden's deconvolution (c)Heatmap showing the correlation of the 1st 10 PCs with cell culture, treatment, individual, RIN , sex, age and the cell type proportions of the 8 cell types.

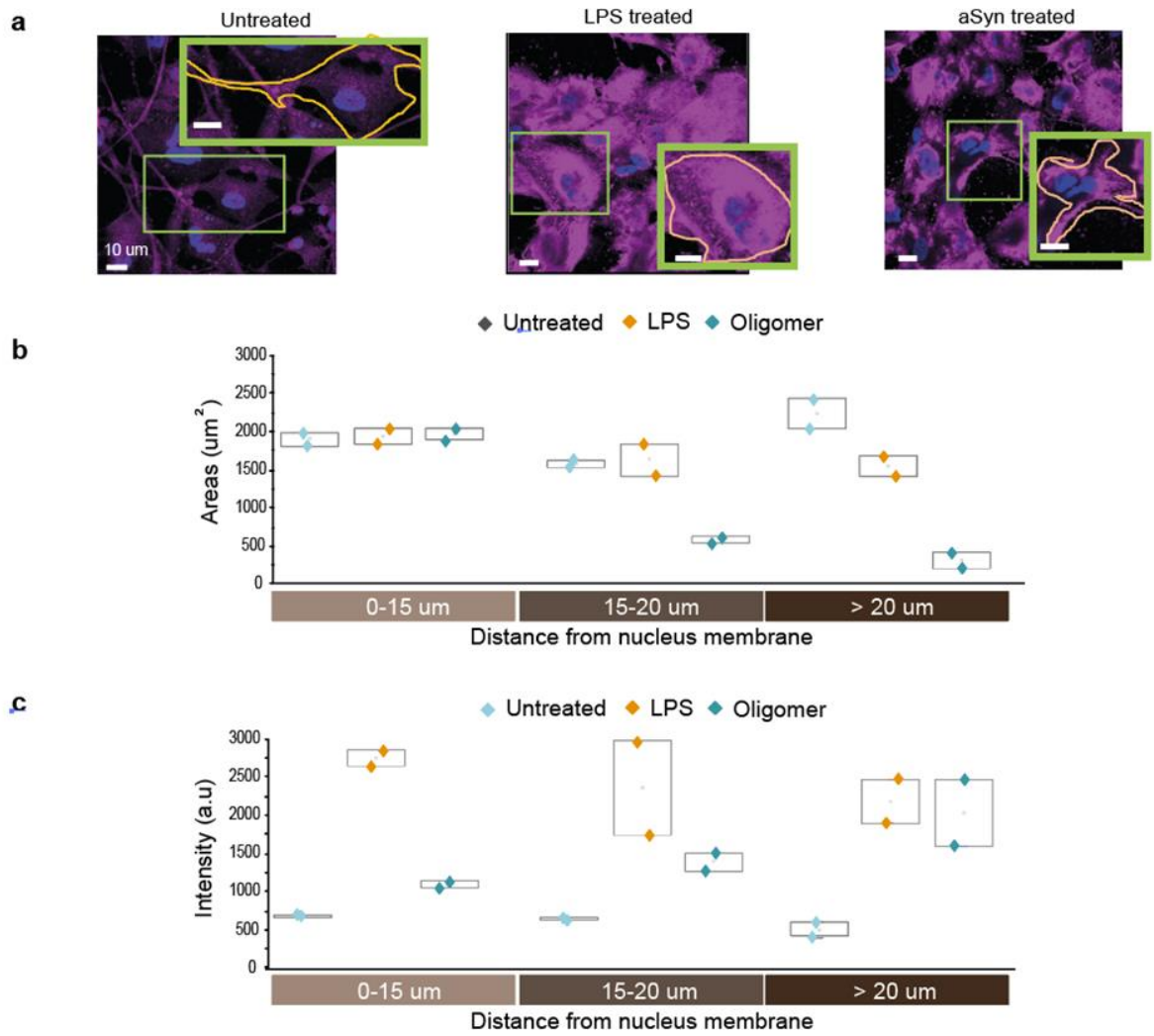

Supp Fig 3

Morphological changes induced in reactive astrocytes on αsyn-O treatment: (a) representative images of astrocytes immune labelled with GFAP demonstrating change in morphology upon stimulation by LPS or αsyn-O. Assessment of morphology by segmentation of astrocytes followed by (b) assessing GFAP pixel area, according to distance from nuclear membrane (measurement of polarity) and (c) intensity according to distance from nuclear membrane.[38,39]

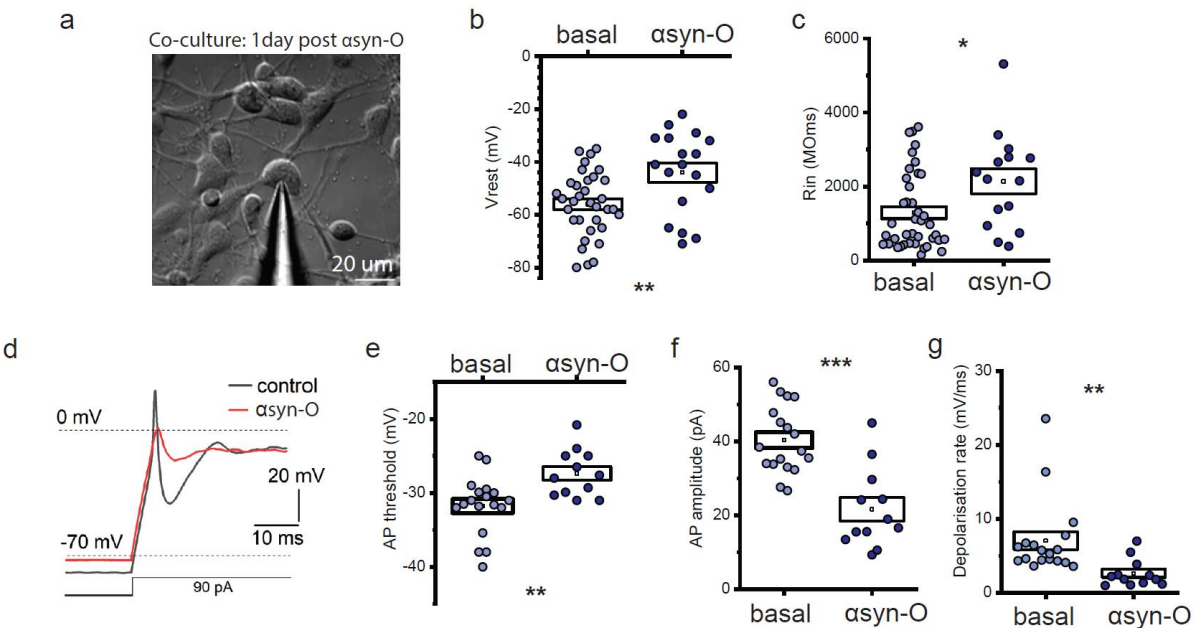

Supp fig 4

(a) DIC image of neuron-astrocytic co-cultures for whole-cell recordings of iPSC-derived neurons 1 day after treatment with exogenous mutant α-syn. (b) Analyses of membrane properties revealed a depolarised Vrest in iPSC-derived neurons at 1-day post-treatment with the pathogenic protein. (c) Cortical neurons exhibited an increased Rin (Input resistance) following the treatment compared with the parameters in control (untreated) co-cultures. (d) Representative recordings of action potential spike in a control co-culture (black) and 1 day post-treatment with the pathogenic α-syn (red). Pathological α-syn impaired the shape and kinetics of individual action potential spikes, as measured for the parameters of threshold (e), amplitude (f) and depolarisation rates (g).

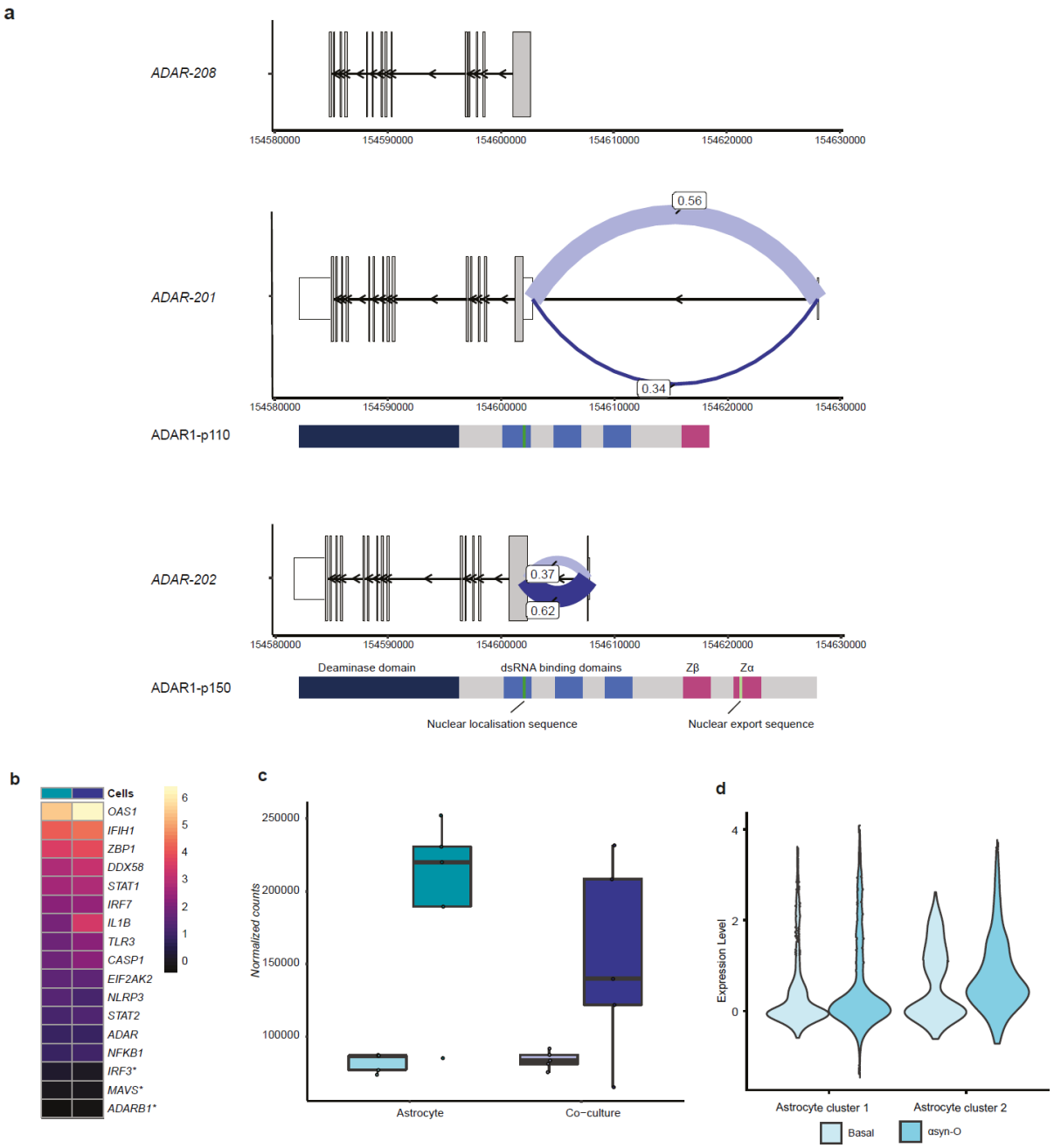

Supp Fig 5

Differential gene expression and splicing of *ADAR* in co-culture on treatment with α-syn oligomers

(a) Splicing in *ADAR* showing alternate isoforms. Junctions are labelled with the junction usage (b) Heatmap showing the $\log_2$FoldChange of the genes, in the innate immune response to dsRNA, (* not significantly differentially expressed at FDR < 5%) in the astrocytes and co-culture on αsyn-O treatment. (c) *ADAR* is differentially expressed in the astrocytes and co-culture on treatment with with α-syn oligomers (d) Expression of *ADAR* in the astrocyte cluster 1 and 2 in the single cell data

1374

1375

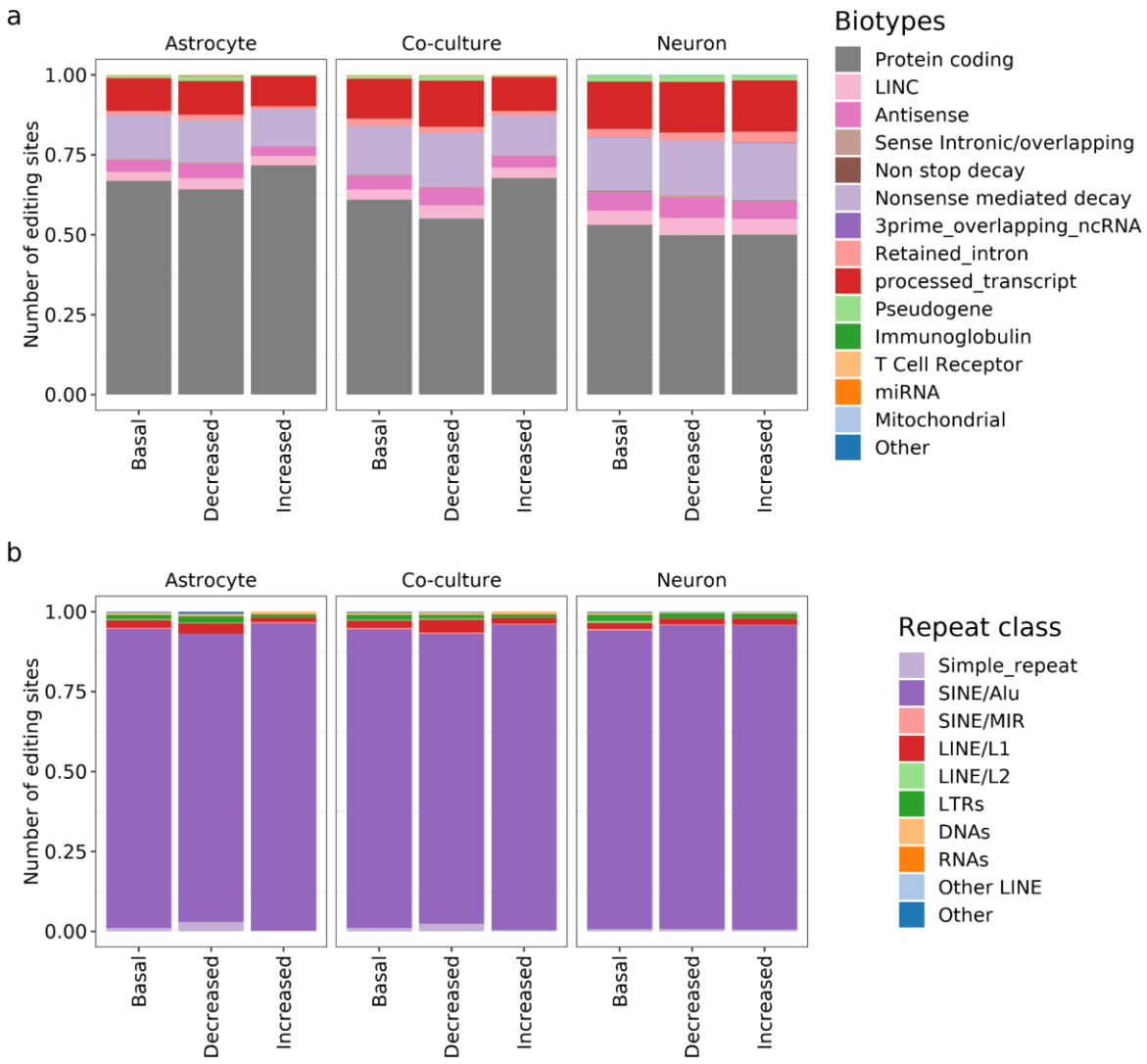

1376

1377 **Supp Fig 6**

1378 Changes in proportion of editing sites with α-synO treatment in astrocytes, co-cultures and neurons showing a)
1379 biotypes annotated with Ensembl Variant Effect Predictor (v93.5). b) Proportion of repeat regions annotated
1380 with RepeatMasker.

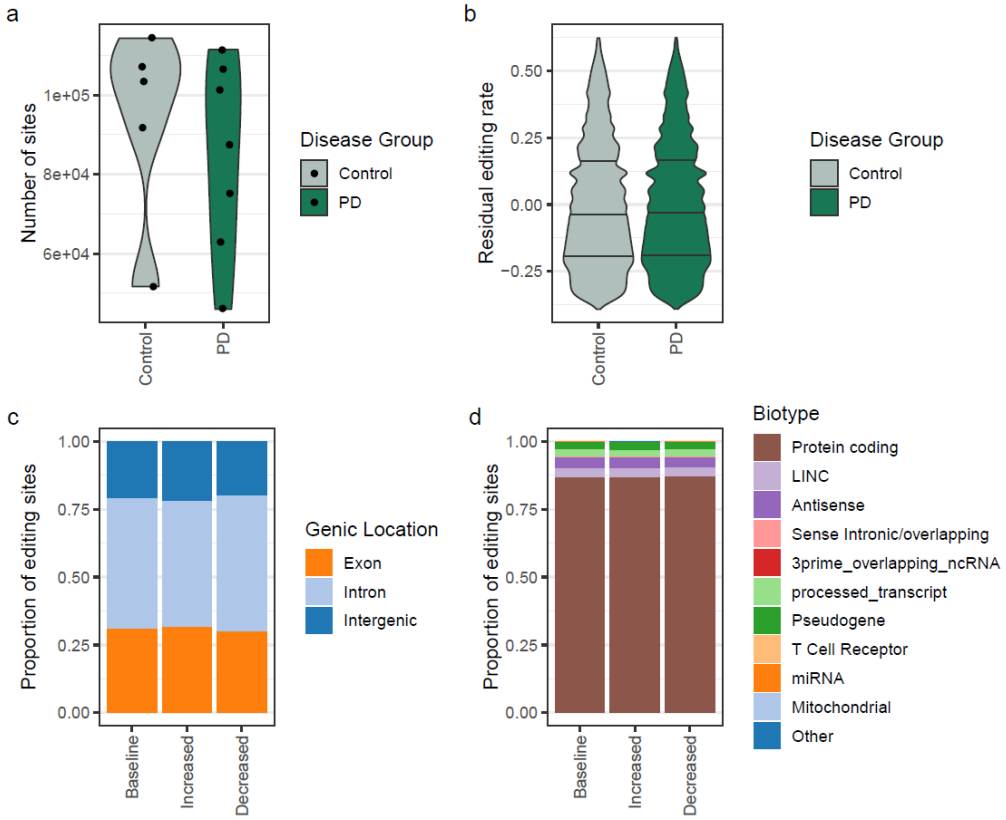

Supp Fig 7

A-to-I RNA editing in PD affected human brain. (a) The total number of sites per brain sample. (b) Residual editing rate after correction for covariates. The change in the proportion of sites that have increased or decreased editing, relative to baseline, in genic location (c), and biotype (d).